Acta Metallurgica Sinica (English Letters) (2023) 36:1573–1602
https://doi.org/10.1007/s40195-023-01597-6

Nanoporous Metals Based on Metallic Glasses: Synthesis, Structure and Functional Applications

Jing Wang[1] · Zhibin Li[1] · Rui Li[2] · Hui Wang[1] · Yuan Wu[1] · Xiongjun Liu[1] · Zhaoping Lu[1]

Received: 4 May 2023 / Revised: 6 July 2023 / Accepted: 10 July 2023 / Published online: 30 August 2023

Abstract
Nanoporous metals have emerged as a new class of functional materials with unique structures and properties. Compared to conventional metals and alloys, nanoporous metals possess a high surface area, unique pore size distribution and enhanced catalytic activity, making them highly desirable for a wide range of applications, such as photonics, sensing, supercapacitors and catalysis. In this review paper, we aim to summarize recent advances in the fabrication, structural regulation and functional applications of nanoporous metals and their composites via the dealloying of metallic glasses. Particularly, we will discuss the factors that affect the nanoporous structure, including precursor composition, dealloying conditions and post-treatment methods. We will also cover topics such as the preparation of immiscible nanoporous metals and the control of hierarchical nanoporous structures. Finally, we will provide a brief overview of the current situation and discuss the current challenges and potential research directions in the field.

Keywords Nanoporous metal · Metallic glass · Dealloying · Functional applications

1 Introduction

1.1 History of Nanoporous Metals

Nanoporous (NP) metals are made of scaffolds on a three-dimensional nanoscale with interconnected ligaments and pores and have attracted extensive attention due to their unique structure and remarkable physicochemical properties [1, 2]. Over the past decades, various approaches have been developed to manufacture NP metals. Among them, dealloying is considered one of the most efficient methods, in which one or more less noble metal atoms are selectively leached from precursor alloys through either chemical or electrochemical corrosion. These more noble metal atoms were then chemically driven to aggregate into interconnected clusters, leading to the formation of a porous skeleton, such as the NP Cu can be prepared by dealloying the Al–Cu [3, 4] or Mn–Cu [5] alloys, and NP Au can be obtained by dealloying the $Au_{35}Si_{20}Cu_{28}Ag_7Pd_5Co_5$ glassy ribbons [6] or Ag–Au alloys [7].

Dealloying, known as depletion gilding, is an ancient technique to utilize an object surface with copper and gold or silver [8]. The fabrication of NP metals by dealloying dates back to the 1920s. In 1927, Raney nickel produced by dealloying Al–Ni alloys was first reported [9], which is still widely used in industrial hydrogenation reactions. Starting from the 1960s, details about dealloyed products and processes were gradually investigated [10]. In the 1980s, the critical potential and composition threshold were revealed as two key parameters to control the dealloying process [11, 12], and a NP metallic structure was finally synthesized in 1990 [13]. Subsequently, Erlebacher et al. systematically investigated the structural evolution, formation mechanism and processing–structure relationship of NP Au [14, 15]. Subsequently, many NP metals/alloys have been successfully

Jing Wang and Zhibin Li have contributed equally to this work.

Available online at http://link.springer.com/journal/40195.

✉ Xiongjun Liu
xjliu@ustb.edu.cn

✉ Zhaoping Lu
luzp@ustb.edu.cn

[1] Beijing Advanced Innovation Center for Materials Genome Engineering, State Key Laboratory for Advanced Metals and Materials, University of Science and Technology Beijing, Beijing 100083, China

[2] Institute of Clean Energy, Yangtze River Delta Research Institute, Northwestern Polytechnical University, Xi'an 710072, China

prepared by dealloying well-designed precursors. In addition, various surface modification strategies have been developed to produce novel NP metal-based composite materials, such as NP Au/MnO_2 [16] and NP Au/polypyrrole [17], hybrid electrodes were fabricated via a facile electroless/electrochemical plating process, and NP bimetallic Cu-Ag alloys were prepared by dealloying the $Mg_{65}Ag_{12.5}Cu_{12.5}Y_{10}$ metallic glass [18].

Porous precious metals with pore size distributions centered below 5 nm exhibit promising application in the fields of electrocatalysis and sensing, owing to their high surface area and electric contact with all surface sites. Such materials have the advantages of nanoparticles with high surface-area-to-volume ratio and few downsides.

1.2 Precursor Alloys

NP metals with bicontinuous and three-dimensional (3D) nanopore structures have been broadly studied due to their multiple advantages, including a high surface area-to-volume ratio, a large number of active sites, mechanical size effect and excellent conductivity [19, 20]. The morphology of NP metals can be adjusted by various parameters, such as the amount of noble elements in the precursor, the parting limit, the electrochemical potential difference between elements, the critical corrosion potential and the composition and temperature of the electrolyte [21]. Common dealloying precursors include Ag–Au and Cu–Mn crystalline alloys [22, 23]. However, there are some limitations of crystalline precursors in the synthesis of NP metals by dealloying, *e.g.*, the small adjustable composition range and inevitable crystalline defects (e.g., dislocations, grain and phase boundaries), such as some microcracks are present in the NP Cu/Au by dealloying the crystalline precursors [24, 25], and the porous is inhomogeneous [26, 27].

Recently, metallic glasses (MGs) have emerged as a new kind of precursor alloys to produce NP metals by electrochemical or chemical dealloying [28]. Compared with crystalline precursor alloys, MGs have unique advantages in obtaining uniform NP structures, owing to their monolithic amorphous microstructure without elemental segregations and crystallographic defects, such as grain boundaries and dislocations [29, 30]. More importantly, many MGs have a wider range of compositions than crystalline solid-solution alloys, which provides greater flexibility in the regulation of nanopores. Also, MGs can be applied to prepare immiscible NP alloys, such as homogenous NP binary Cu-Ag alloys, even though Ag and Cu are immiscible with a positive mixing enthalpy [31, 32]. Therefore, numerous attempts have been made to fabricate NP metals (Ni, Cu, Pd, Ag and Au) by dealloying MG precursors [33].

In this brief review, we aim to summarize recent advances in the fabrication, structural regulation and functional applications of NP metals and their composites via the dealloying of MGs. We discussed the factors that affect NP structure, including precursor composition, dealloying conditions and post-treatment methods. Also, the application of NP materials, in the fields of photonics, sensing, hydrogen evolution, oxygen catalysis and supercapacitors (Fig. 1), has been elaborated in detail. Finally, we provided fundamental insights and the most potential directions for research in the future. These insights might be helpful for scientists to develop advanced NP materials for energy storage and conversion.

2 Synthesis and Structural Manipulation of NP Metals

2.1 Synthesis of NP Metals

During dealloying, the less noble metal atoms are selectively leached from precursor alloys by chemical or electrochemical corrosion, and the residual more noble metal atoms are chemically driven to form interconnected clusters, resulting in the formation of a porous skeleton. In general, the dealloying processes can be divided into chemical dealloying and electrochemical dealloying.

2.1.1 Chemical Dealloying

Chemical dealloying is frequently conducted in suitable acid or alkaline solutions. A proper and more noble

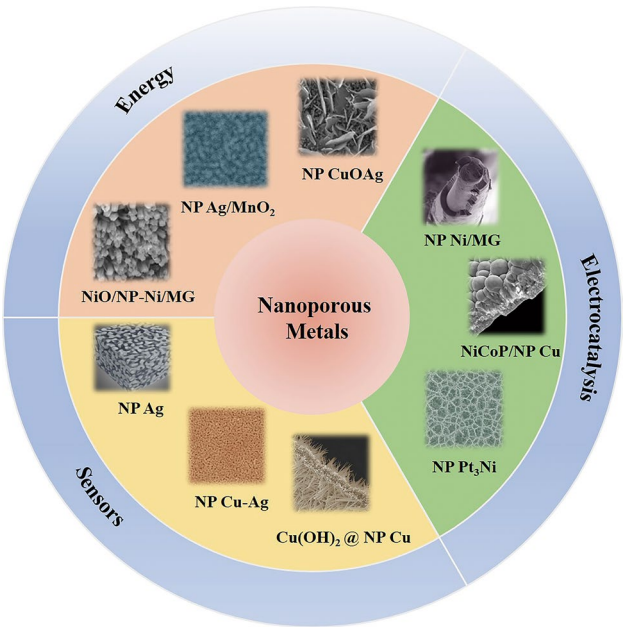

Fig. 1 Schematic of NP materials for energy storage, sensors and electrocatalysts

metal-based multicomponent alloy is first selected or designed as the initial precursor. Then, the less noble metal atoms are selectively leached from the precursor alloys. Meanwhile, the more noble metal atoms are chemically driven to form a 3D NP structure. The chemical dealloying process is easy to operate and conducive to a large-scale synthesis.

MGs that possess a homogeneous atomic structure and have no crystallographic defects show significant advantages as precursor alloys for the fabrication of NP metals. Meanwhile, adjustable constituent elements are also beneficial for achieving desirable pore characteristics and overall properties. Several attempts have been made to prepare NP metals by dealloying MGs. NP Pd, Au, Ag, Cu and Ni metal/metal-oxide composites were fabricated by dealloying Pd–, Au–, Mg–, Cu–, Zr– and Al-based MGs [30, 34–38]. In particular, Li et al. fabricated NP Ag with tunable porosity by chemically dealloying Ag-based MGs in an HCl solution. After dealloying, an open and bicontinuous NP structure was observed with predominant ligament and pore sizes of ~ 65 and ~ 61 nm, respectively, as shown in Fig. 2.

HCl solutions with different concentrations exhibit various critical dealloying times for achieving optimal NP structures when the surface dealloying process is completed. Figure 3a–d shows the typical surface morphology of the dealloyed $Ag_{45}Mg_{35}Ca_{20}$ MG in 0.025, 0.1, 1 and 12 mol L^{-1} HCl solutions for different critical leaching durations. Obviously, a shorter critical dealloying time was required to achieve a uniform NP structure on the glass surface in HCl solution with a higher concentration, leading to a finer pore structure. Specifically, as the HCl solution concentration increased from 0.025 to 12 mol L^{-1}, the critical dealloying time dropped from 8 h to 10 min, and accordingly, the ligament size decreased dramatically from ~ 81 (Fig. 3a) to ~ 18 nm (Fig. 3d). Similarly, three-dimensional NP Cu films with tunable thicknesses of ~230 nm to ~2.2 μm were fabricated by chemical dealloying of Cu-Zr-Al MGs at room

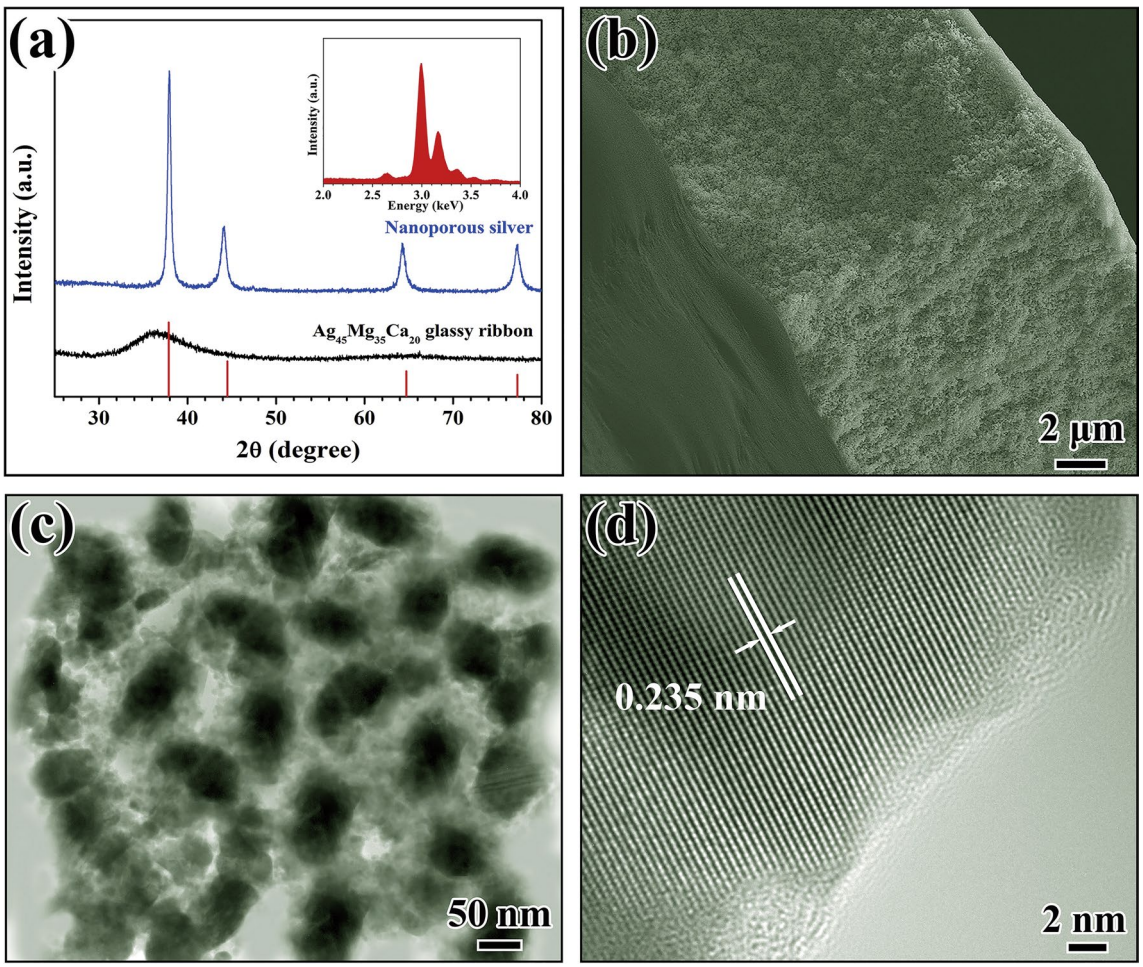

Fig. 2 **a** XRD pattern, **b** cross-sectional (scanning electron microscopy) SEM image, **c** TEM image, **d** high-resolution transmission electron microscopy (HRTEM) image of the resultant NP Ag by dealloying the $Ag_{45}Mg_{35}Ca_{20}$ metallic glass in 0.05 mol L^{-1} HCl aqueous solution for 4 h at room temperature. Reprinted with permission from [39]

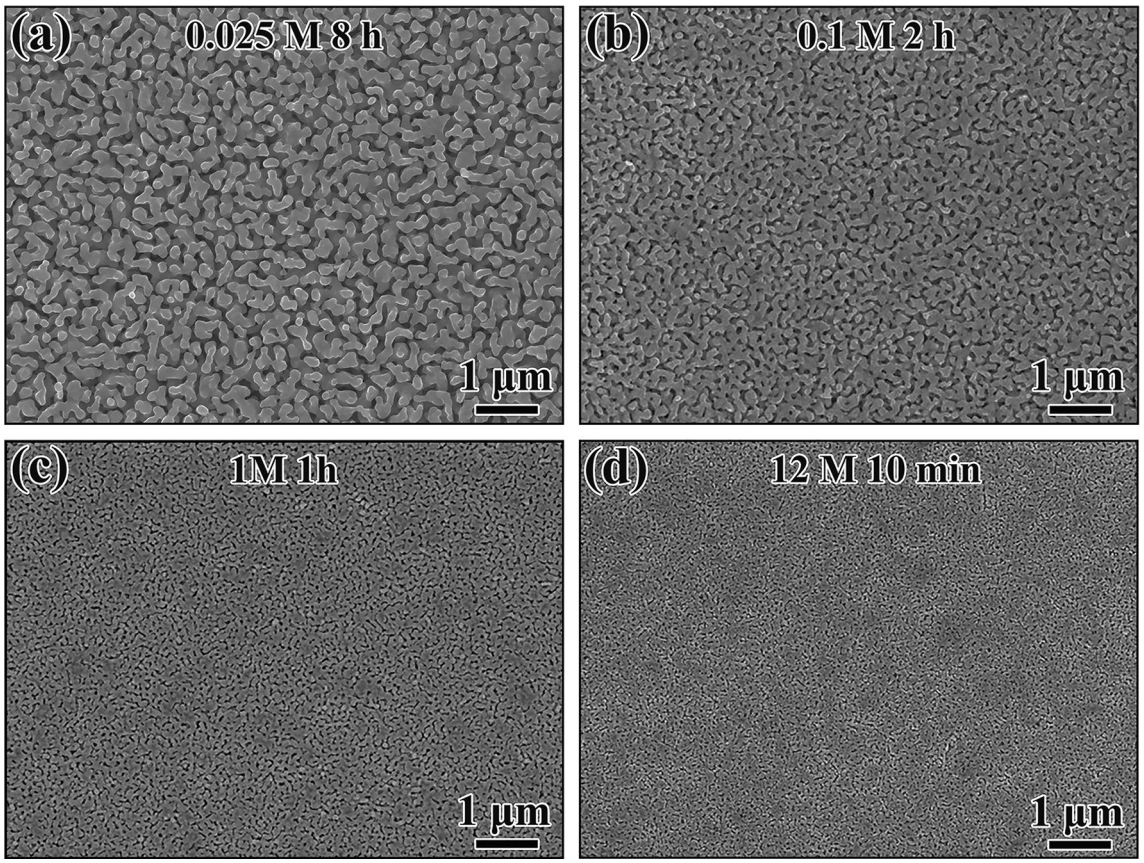

Fig. 3 Surface morphologies of the resultant NP silver by dealloying the $Ag_{45}Mg_{35}Ca_{20}$ MG at room temperature in **a** 0.025 mol L^{-1} HCl solution for 8 h, **b** 0.1 mol L^{-1} HCl solution for 2 h, **c** 1 mol L^{-1} HCl solution for 1 h, **d** 12 mol L^{-1} HCl solution for 10 min, respectively. Reprinted with permission from [39]

temperature in a HF solution [38]. Figure 4 shows structural features of a typical NP Cu thin film prepared by chemical dealloying of $Cu_{60}Zr_{35}Al_5$ MG. The XRD pattern in Fig. 4a reveals that the amorphous halo of the glassy precursor is replaced by sharp peaks corresponding to fcc Cu after dealloying, indicating that Al and Zr were completely leached out from the glassy precursor. NP Ni/MG wire with a hierarchically porous structure was also successfully prepared by chemical dealloying of specially designed Ni-based MG wire in the 0.1 mol L^{-1} HF solution [40]. As shown in Fig. 5a and b, the surface of the dealloyed $Ni_{40}Zr_{40}Ti_{20}$ MG wire was composed of a hierarchically porous configuration, with micrometer slits (0.4–1.4 μm) (Fig. 5c) and nanometer pores interleaved (6–50 nm).

Recently, NP bimetallic alloys have attracted strong interests due to their potential applications. Zhang et al. synthesized a NP Pd–Ag alloy by dealloying an amorphous PdAgCuSi alloy in HNO_3/HF mixed acidic solution to remove less noble Cu and Si elements [41]. Li et al. synthesized a three-dimensional NP Ag–Cu bimetallic alloy with uniform chemical composition fabricated by dealloying Mg–Ag–Cu–Y MG in the 0.04 mol L^{-1} H_2SO_4 aqueous solution. NP bimetallic Ag–Cu alloy with an ultrafine ligament size (below 20 nm), a large specific surface area (above 11.18 m^2 g^{-1}) and high oxidation resistance was employed to inhibit the growth of gram-negative *E. coli* and gram-positive *S. aureus* [32, 42].

NP metals and alloys with bicontinuous and 3D nanopore structures can be obtained using MGs as the precursors by selectively dissolving less stable atoms through galvanic corrosion based on the disparity of electrode potentials among the constituent elements [28]. In addition, NP amorphous alloys were developed by removing the phase-separated glassy precursors [43]. Jiao et al. synthesized NP multicomponent MG by combining selective Y-rich glassy phase dissolution and passivation of a spinodal decomposed glassy precursor [44]. As shown in Fig. 6, a three-dimensional NP structure with an average pore size of ~25 nm uniformly spans the thickness of the ribbons. Owing to its large specific surface area and high hydrogen diffusivity, the NP MG shows superb hydrogen uptake performance.

The aforementioned results indicate that chemical dealloying is a facile and rapid strategy to fabricate NP metals. However, two limitations exist for this method: the first is the

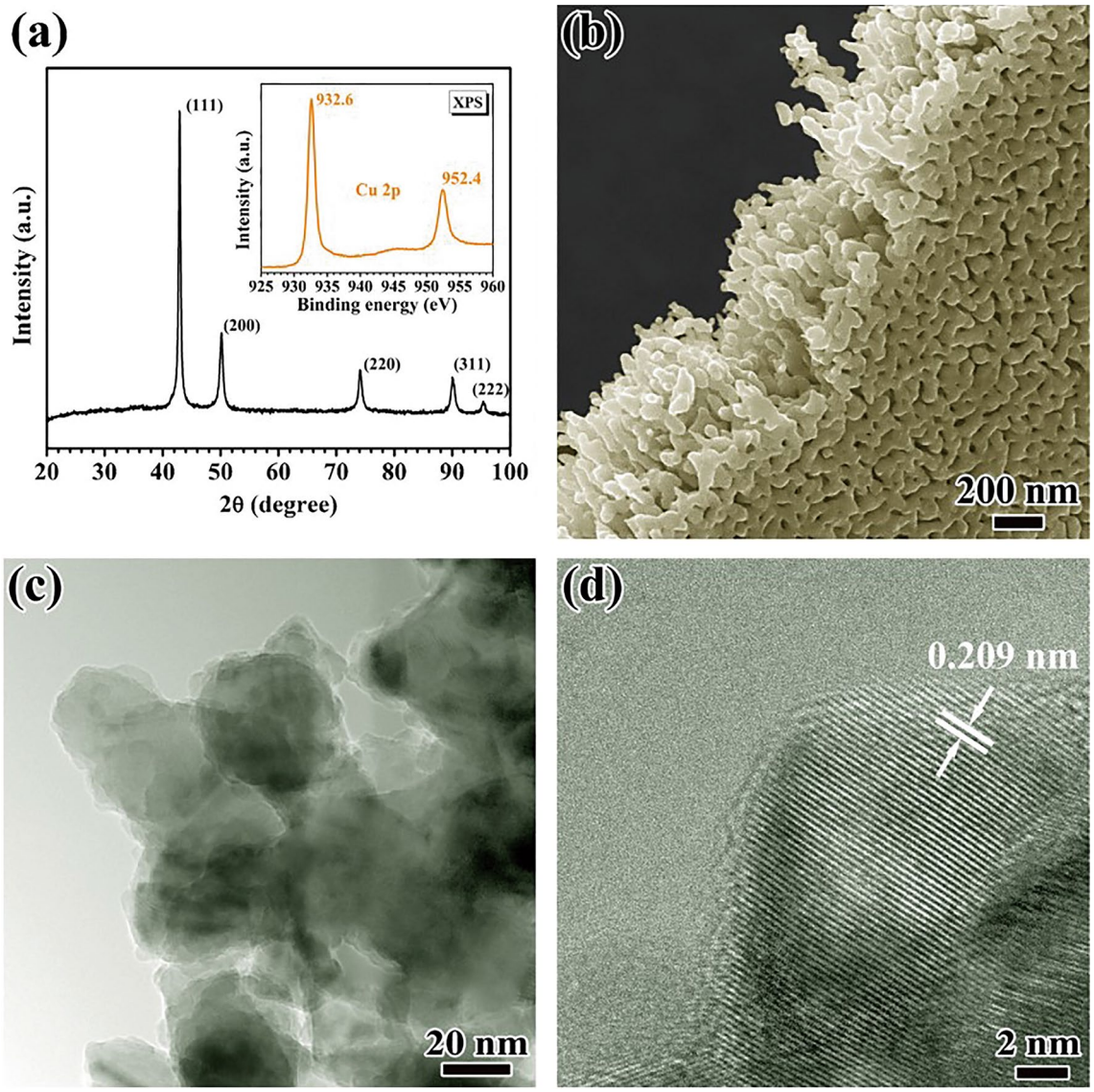

Fig. 4 **a** XRD pattern of the NP Cu thin film fabricated by chemical dealloying in 0.005 mol L^{-1} HF solution for 24 h, and the inset is the corresponding XPS spectra of Cu-2*p*. **b** Cross-sectional image of the NP Cu thin film. **c** TEM, **d** HRTEM images of the ligaments of the NP Cu thin film, respectively. Reprinted with permission from [38]

excessive and uncontrollable corrosion which results from the necessary use of strong acid or alkaline solutions in the dealloying process. The other is the difficulty in controlling surface morphology because the active atoms on the alloy surface are usually etched randomly. As a result, other methods are needed so as to control the dealloying process and the morphology of NP metals for various applications.

2.1.2 Electrochemical Dealloying

Electrochemical dealloying is another effective approach to selecting the most active species from alloys and form an interconnected porous metal structure [45, 46]. The parting limit and critical potential are considered as two key factors in electrochemical dealloying [47]. The parting limit refers to the limiting concentration at which the alloy component can be dealloyed, whilst the critical potential refers to the electrode potential threshold that must be overcome for the electrochemical dissolution of the active metal component in the precursor alloy. Compared with chemical dealloying, the chemical composition of NP noble metal-based alloys is more easily controlled in electrochemical dealloying. In the study of Ou et al., the $Fe_{60}Pt_{10}B_{30}$ amorphous alloy precursor was used to fabricate a NP Pt-Fe alloy with a single fcc Pt-Fe phase by electrochemical dealloying in 0.1 mol L^{-1} H_2SO_4 solution [48]. The NP Pt-Fe alloy was reported to have a fine

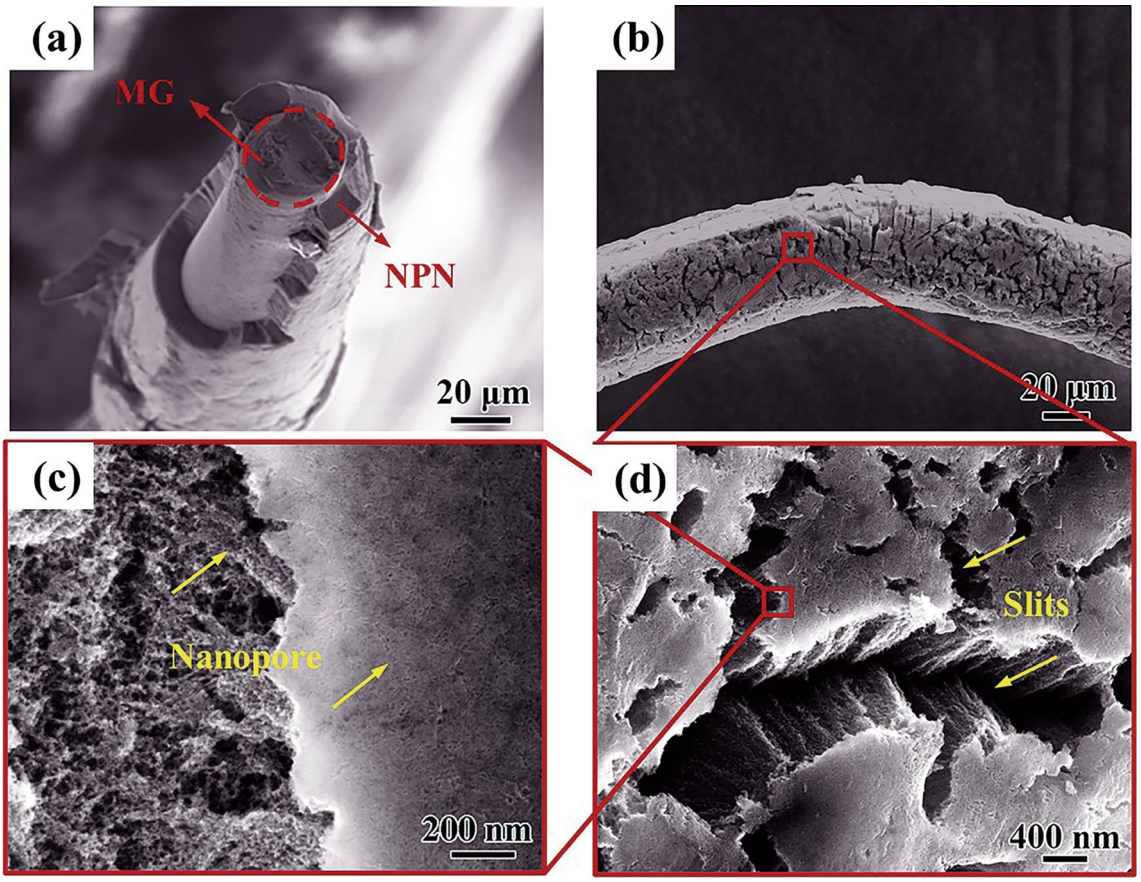

Fig. 5 Characterization of NP Ni/MG. **a** SEM image of the cross section of the dealloyed NP Ni/MG wire. **b**, **c**, **d** Surface morphologies of the dealloyed $Ni_{40}Zr_{40}Ti_{20}$ MG wire. Reprinted with permission from [40]

bicontinuous ligament/channel structure with sizes of ~ 7 nm and ~ 5 nm. Similarly, a novel Pd-based NP structure consisting of amorphous nanoparticles and interconnected conduits was successfully fabricated by electrochemical dealloying of $Pd_{32}Ni_{48}P_{20}$ metallic glass at a relatively low potential in sulfuric acid solution [49]. In addition, Tanaka et al. synthesized NP Pd by dealloying a $Pd_{30}Ni_{50}P_{20}$ MG [50]. A requisite NP Pd catalyst was fabricated using a classical three-electrode setup by electrochemically dealloying $Pd_{30}Ni_{50}P_{20}$ MG ribbons with approximately 15 mm thickness for 2 h in 1 mol L^{-1} H_2SO_4. In addition, NP binary Au–Pd with bicontinuous and 3D nanopore structures was also fabricated by electrochemical dealloying of $Au_{30}Si_{20}Cu_{33}Ag_7Pd_{10}$ MG [51].

2.2 Regulation of NP Structure

2.2.1 Dealloying Conditions

The microstructure of NP metals is strongly dependent on the dealloying time and temperature. Li et al. investigated dynamic changes in the pore characteristics of NP Ag under various dealloying conditions and established the correlation between ligament size and dealloying parameters [39]. Figure 7a–f illustrates the microstructure evolution during the dealloying of the $Ag_{45}Mg_{35}Ca_{20}$ MG at different dealloying times (2–36 h) in 0.025 mol L^{-1} HCl aqueous solution at room temperature. A complete NP structure with an average ligament size of ~ 81 nm was obtained after 8 h dealloying of the glassy precursor. The ligament size tends to coarsen with the further increase of dealloying time. In particular, when the dealloying time was extended to 24 h, the typical ligament length was prolonged to 90–100 nm. When the dealloying time increased to 36 h, the NP structure eventually collapsed due to the coarsening effect.

In addition to dealloying time, the dealloying temperature is another important parameter to control the microstructure of NP metals. The temperature effect on the nanoporosity was investigated by varying the dealloying temperature from 273 to 368 K. Figure 8a–d illustrates the surface and cross-sectional (see insets in the figure) morphologies of the synthesized samples after dealloying in 0.05 mol L^{-1} HCl solution for 4 h at 273, 298, 323, 348 and 368 K, respectively. All the samples showed uniform

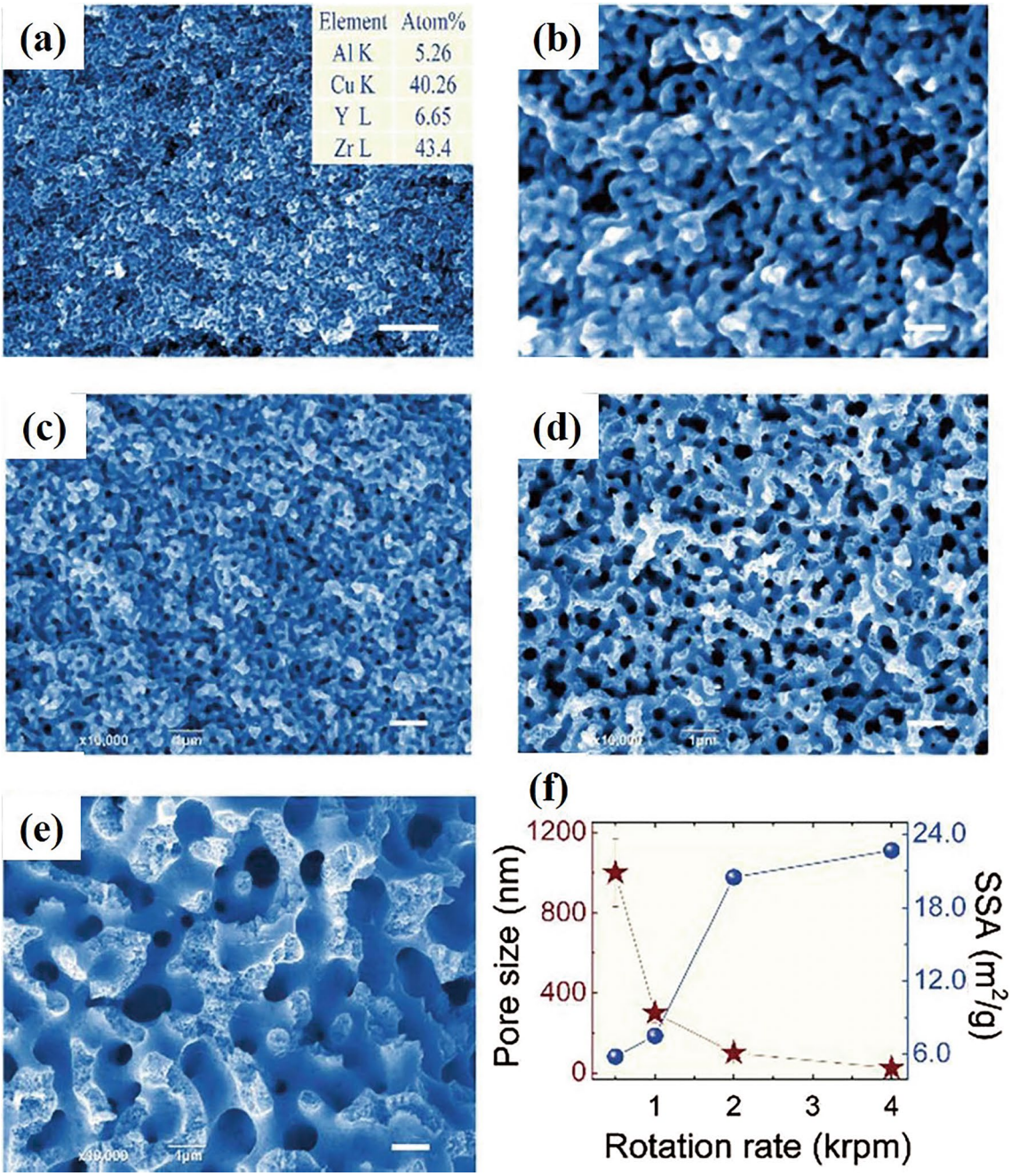

Fig. 6 Morphology of the porous alloy. **a** and **b** SEM images of the residual alloy (panel b is highly magnified). The speed of the copper roller is 4 K rpm. The pore sizes were tuned by the cooling rate and characterized by the speed of the copper roller: **c** 2 K, **d** 1 K, **e** 500 rpm. **f** Variation in the pore size and specific surface area (SSA) with the rotation rates of the copper roller. Scale bars are 500 nm for panel a, 100 nm for panel b, and 1 μm for panels c-e. Reprinted with permission from [44]

and continuous nanoporosity, and the characteristic length scale (i.e., pore and ligament size) increased with increasing dealloying temperature. However, when the temperature increased to 368 K, the morphology of the NP structure changed and the ligaments consisting of irregular Ag particles (50–80 nm) agglomerated into islands with a size of ~ 1.2 mm.

The correlation between ligament size and dealloying parameters was established by investigating the dynamic change in pore characteristics of NP Ag under various dealloying conditions. The evolution behavior of the ligament could be described based on a diffusion-based growth kinetic model. A nonlinear relationship was found between ligament growth and the dealloying temperature or time, similar

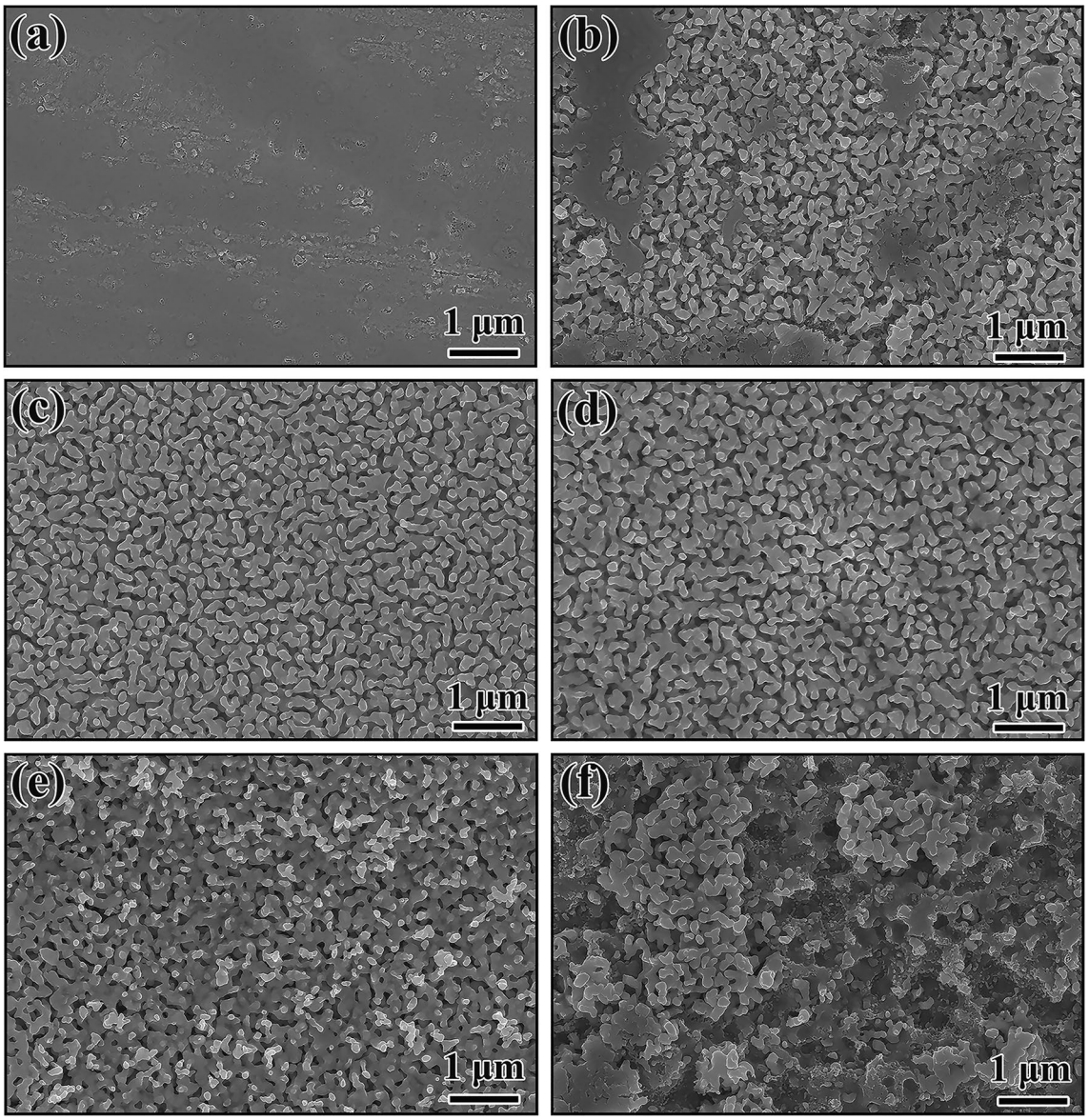

Fig. 7 Surface morphologies of the Ag NPs produced by chemical dealloying in a 0.025 mol L^{-1} HCl aqueous solution for **a** 2 h, **b** 6 h, **c** 8 h, **d** 12 h, **e** 24 h, **f** 36 h at room temperature. Reprinted with permission from [39]

to isothermal grain growth in polycrystalline materials [52, 53].

$$dn = KD_0 \exp\left(\frac{-E_a}{RT}\right)t = KtDs, \tag{1}$$

$$Ds = D^0 \exp\left(\frac{-E_a}{RT}\right), \tag{2}$$

where n is the coarsening exponent, d is the ligament size, K and D_0 are constants, R is the gas constant, T is the dealloying temperature and E_a is the activation energy for ligament formation and coarsening. The coarsening exponent n can be measured by plotting the ln$d$ vs ln$t$ curves, i.e., the reciprocal of the slope in Fig. 9b. The linearity of the curves indicates a thermal activation process of ligament growth. Therefore, the curve of $\ln(d^n/t)$ versus $(RT)^{-1}$ (Fig. 9c) was plotted to estimate the activation energy, which was determined to be ~ 63.5 kJ mol^{-1}, suggesting that the diffusion growth model can accurately describe the influence of the dealloying temperature on the growth of Ag ligament. This finding implies that the dimension of the NP structure can be tuned and controlled by optimizing the dealloying conditions.

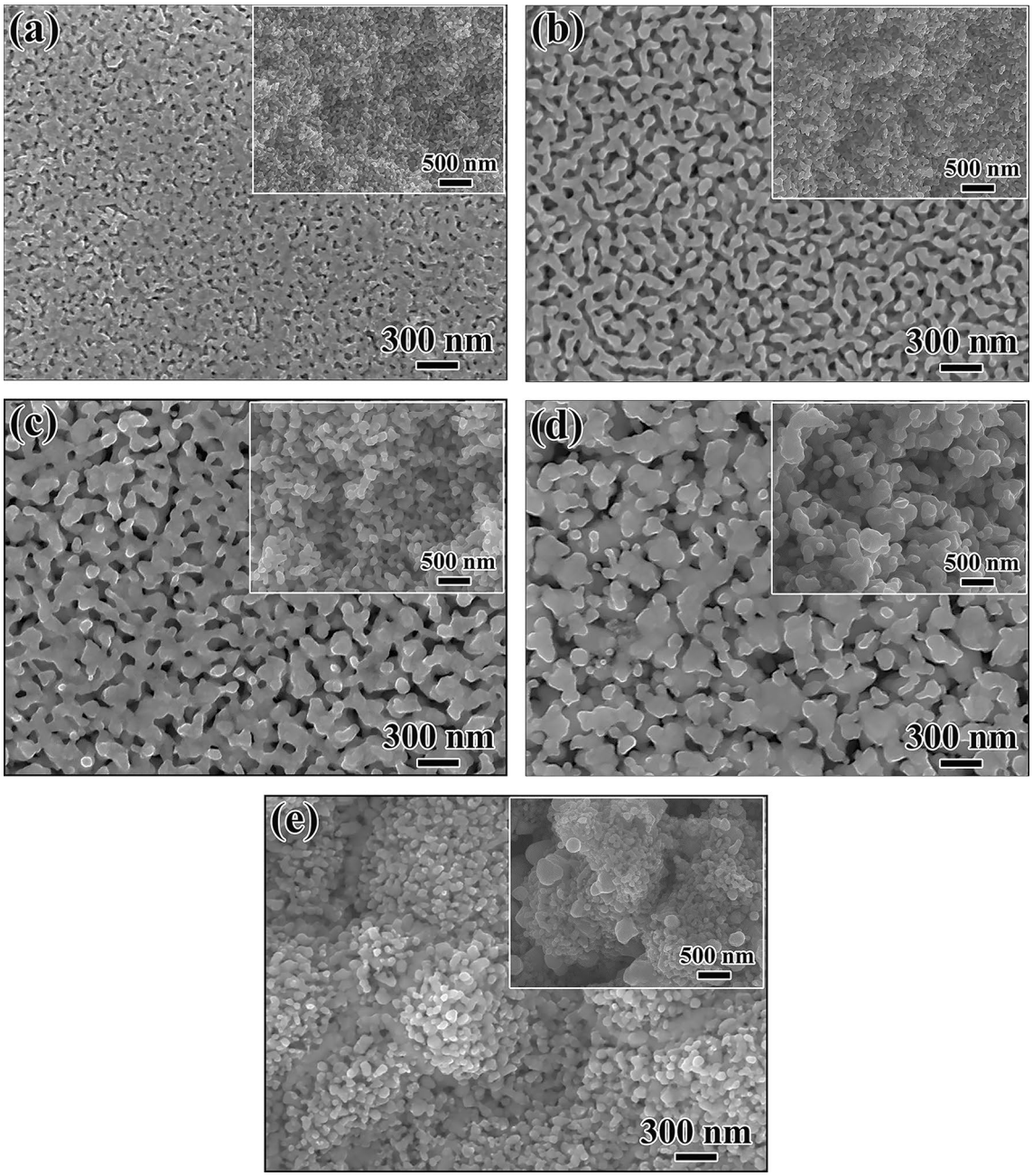

Fig. 8 Microstructures of the resultant NP Ag by dealloying the $Ag_{45}Mg_{35}Ca_{20}$ MG in the 0.05 mol L^{-1} HCl solution for 4 h at different temperatures: **a** 273 K, **b** 298 K, **c** 323 K, **d** 348 K, **e** 368 K. The insets in each image show the corresponding cross section of the NP silver. Reprinted with permission from [39]

2.2.2 Alloying Effect

The composition and structure of the precursors play important roles in the formation of NP metals [54]. In addition, the composition range for glass formation is relatively large, which provides the possibility for preparing the solutions with a variety of immiscible elements. Wang et al. fabricated 3D immiscible NP Cu–Ag with tunable porosity by dealloying Cu–Zr–Al–Ag MGs [31]. The addition of Ag substantially slowed down the dealloying process, and a composition threshold existed (~ 10 at.% Ag) for the formation of uniform NP structure using the Cu–Zr–Al–Ag glassy precursor. In addition, the critical time of the formation of NP Cu–Ag with different Ag contents was determined at room temperature in the 0.01 mol L^{-1} HF solution. As shown in Fig. 10a–e, 3D bicontinuous NP metals were formed in the samples with an Ag content less than 10 at.% after dealloying. The surface area increased linearly with

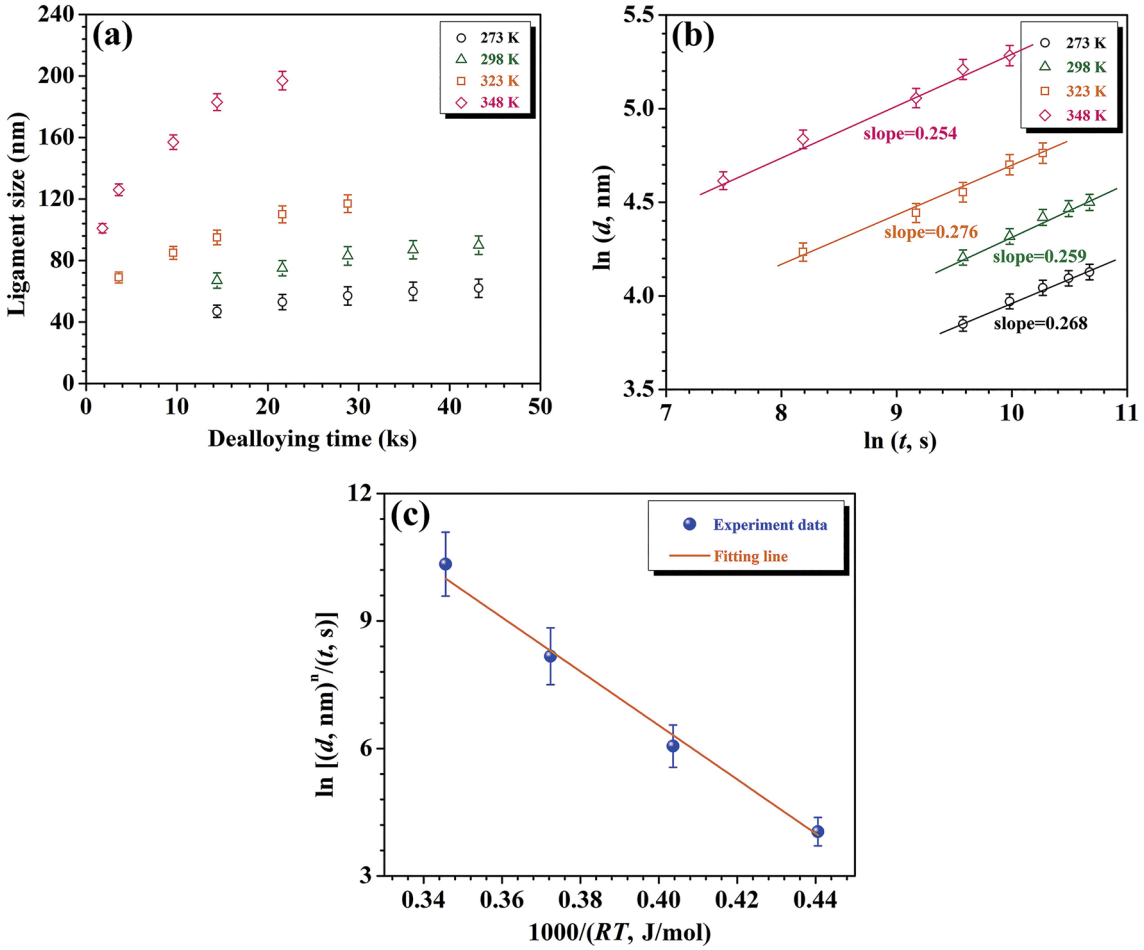

Fig. 9 **a** Dependence of ligament size on dealloying time at different temperatures. **b** Plot of ln$d$ vs ln$t$ at each dealloying temperature for deriving the coarsening exponent. **c** Plot of ln (d^n/t) vs $(RT)^{-1}$ for deriving the activation energy. Reprinted with permission from [39]

increasing Ag, whilst the pore size decreased drastically from 50.1 to 11.3 nm, indicating that the increase in the Ag content of the precursors caused ligament thinning.

It is important to note that there exists a composition threshold for this MG precursor to form a uniform NP structure. When the Ag content exceeds the threshold, an inhomogeneous NP structure will be formed, accompanied by obvious cracks and nanoparticle precipitation on the surface (Fig. 11). A competition mechanism in the formation of the immiscible two noble metals was proposed (Fig. 12). In particular, repulsive interactions between Cu and Ag atoms occurred during the dealloying due to a positive mixing enthalpy, resulting in a slower nucleation and aggregation in NP Cu–Ag than in NP Cu.

Microalloying exerts a great impact on the morphology of NP metals. In the study of Li et al. [55], a honeycombed NP $Pt_{75}Ni_{25}$ with large contact areas was fabricated by surface dealloying of Ni-based MG precursors with the addition of a small amount of Pt (3 at. %) into a Ni-based MG precursor. In particular, a Pt-rich honeycombed structure can be prepared by alloying a small amount of Pt into the MG precursor (Fig. 13).

2.2.3 Composite Materials Based on NP Metals

The properties of monolithic NP metals could be improved by the synergistic effect of different constituent elements in multicomponent alloys. In addition, NP metals can be used as suitable substrates for synthesizing composite materials to enhance their performance. Li et al. prepared a free-standing $Cu(OH)_2$ nanograsses@NP Cu hybrid with a 3D hierarchical nanostructure by chemically dealloying the $Cu_{60}Zr_{35}Al_5$ glassy precursor. Meanwhile, the resultant NP Cu was oxidized in alkaline solution to grow self-aligned $Cu(OH)_2$ nanograsses (Fig. 14) [56]. Such a cost-effective hierarchical hybrid structure requires a unique combination of NP Cu with high conductivity and $Cu(OH)_2$ with high electrocatalytic activity, which achieved a faster redox reaction and electron transport, resulting in superb electrocatalytic activities for glucose oxidation.

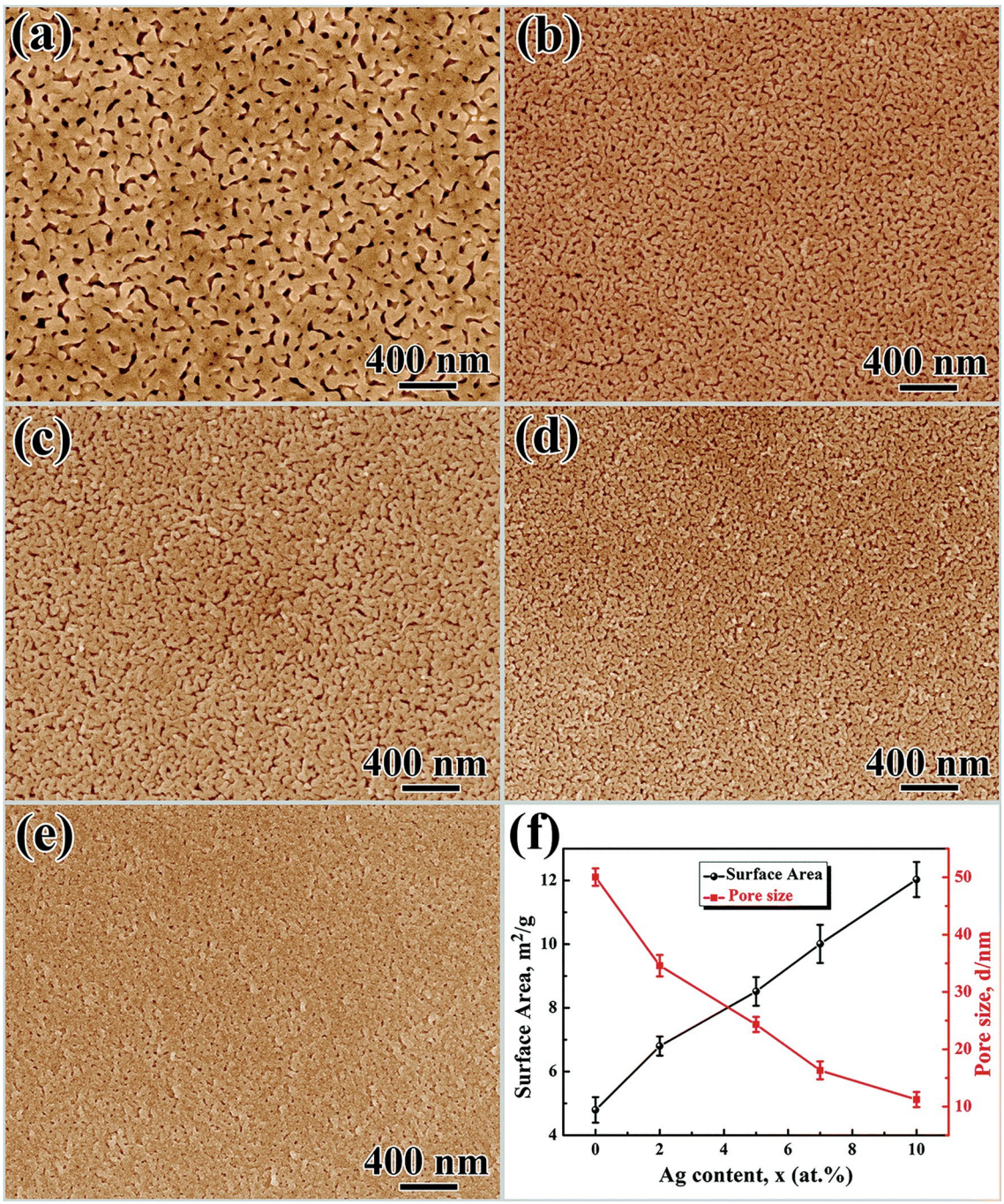

Fig. 10 SEM images of the as-dealloyed samples. **a** $Cu_{50}Zr_{45}Al_5$, **b** $Cu_{50}Zr_{43}Al_5Ag_2$, **c** $Cu_{50}Zr_{40}Al_5Ag_5$, **d** $Cu_{50}Zr_{38}Al_5Ag_7$, **e** $Cu_{50}Zr_{35}Al_5Ag_{10}$. **f** Variation in the surface area and pore size as a function of Ag. Reprinted with permission from [31]

In the study of Li et al., CuO nanowire array/NP Cu composite materials were fabricated by the dealloying of $Cu_{60}Zr_{35}Al_5$ glassy ribbons and subsequent thermal oxidation [57]. The CuO nanocomposite exhibited a hierarchical nanostructure consisting of a well-aligned CuO nanowire array and NP Cu substrate with a continuous nanoporosity (Fig. 15). Compared with commercial CuO nanoparticles, the resulting nanocomposite product exhibited a high internal surface area and superior degradation performance for methylene blue in the presence of H_2O_2.

In addition, electroless plating or electroplating on the surface of NP metals is also feasible approach to preparing composite materials. Li et al. successfully synthesized NP Ag/MnO_2 composites by electroless plating of

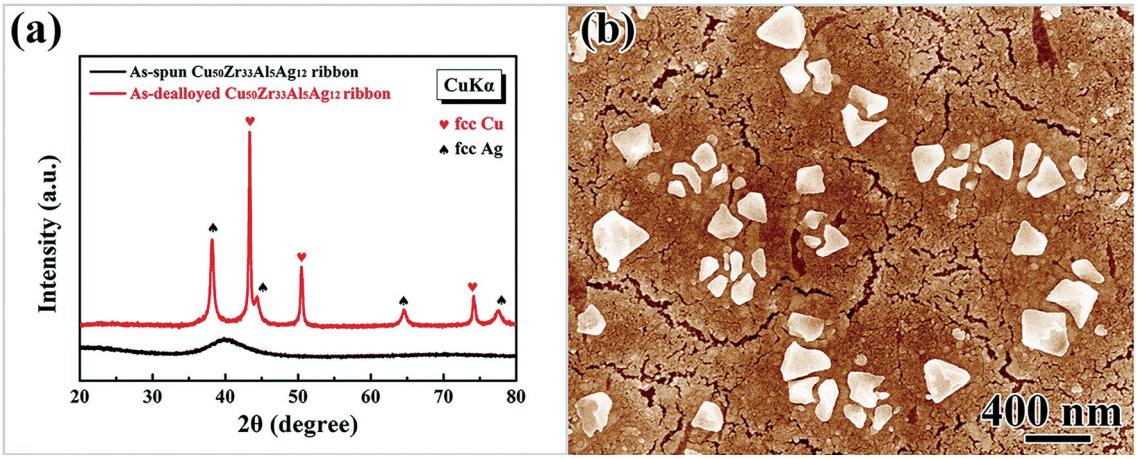

Fig. 11 **a** XRD patterns of the as-spun and as-dealloyed $Cu_{50}Zr_{33}Al_5Ag_{12}$, **b** SEM images of the NP Cu–Ag fabricated by dealloying $Cu_{50}Zr_{33}Al_5Ag_{12}$ MG in the 0.01 mol L^{-1} HF aqueous solution at room temperature for 40 h. Reprinted with permission from [31]

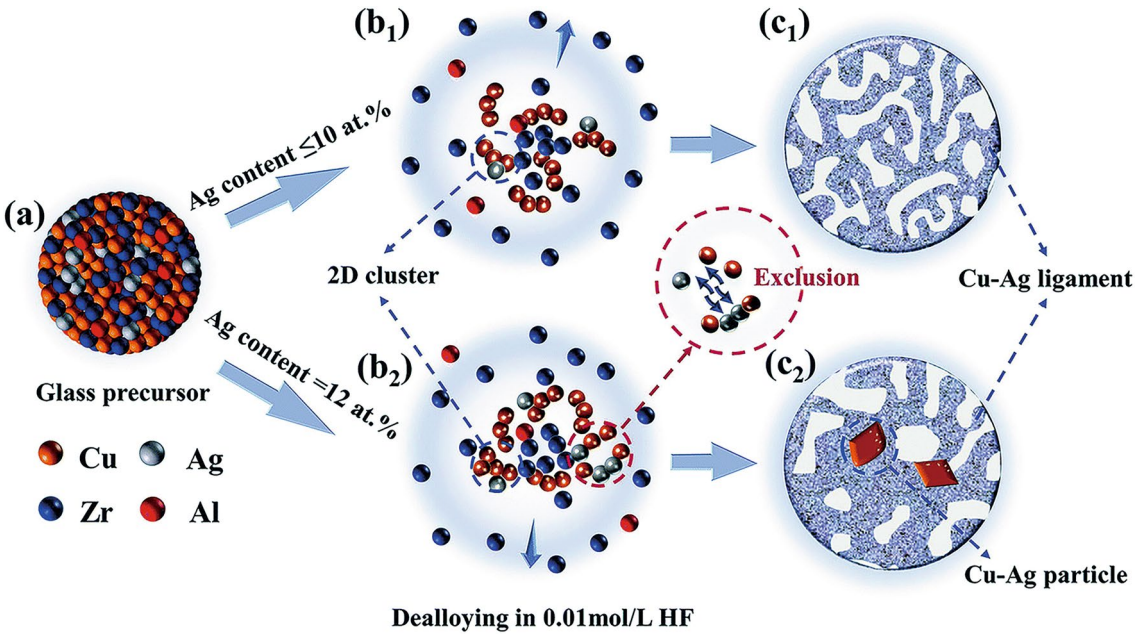

Fig. 12 Schematic illustration of the dealloying mechanism in the Cu–Zr–Al–Ag MGs. **a** Amorphous precursor, **b** dissolution of Zr and Al atoms, agglomeration of Cu and Ag into tiny clusters, **c** formation of porous structures. The red circle in $\mathbf{b_2}$ illustrates the mutually exclusive process between the Cu and Ag atoms. Reprinted with permission from [31]

nanocrystalline MnO_2 on NP Ag (Fig. 16) [58]. Homogeneous NP Ag with an open nanopore structure provided high electrical conductivity and served as the electron collector and greatly enhanced the electron–proton transport of the MnO_2 nanocrystals, resulting in the formation of active MnO_2 with a high specific capacitance of ~ 80% of the theoretical value. Moreover, self-supporting NiCoP/NP Cu composites were fabricated by electrochemical deposition of NiCoP microspheres on NP Cu (Fig. 17) [59]. Compared to the Cu foil, the NP Cu substrate with a 3D bicontinuous network structure facilitated the uniform nucleation of NiCoP and prevented the aggregation of deposited NiCoP microspheres, resulting in an outstanding hydrogen evolution reaction performance of the NiCoP/NP Cu composites.

After the dealloying of Ti–Zr–Cu–Ni–Sn MGs, the resultant NP Cu was soaked in dehydrated ethanol to obtain NP Cu@Cu_2O nanobelt composites [60]. The fabricated Cu_xO or Cu_xO/Ag_2O nanowire composites were grown on a NP substrate by dealloying Cu–Zr–Ag MGs, followed by anodizing and calcination [61]. Thus, NP metals can be used as effective substrates for NP composite materials with prominent performance.

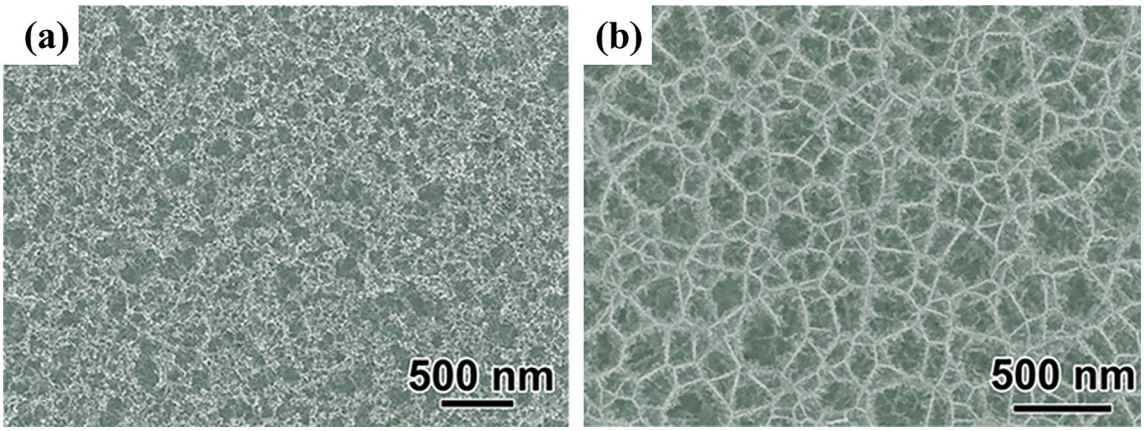

Fig. 13 **a** Surface morphology of the dealloyed $Ni_{40}Zr_{40}Ti_{20}$ MG ribbon. **b** Surface morphology of the dealloyed $Ni_{40}Zr_{40}Ti_{17}Pt_3$ MG ribbon. Reprinted with permission from [55]

3 Applications of NP Metals

NP metals have the advantages of a large surface area, high porosity, good electrical conductivity, abundant active sites, etc. Therefore, NP metals have great potential to be utilized in various applications. Representative applications of NP metals and their composites include surface-enhanced Raman spectroscopy (SERS), sensors, supercapacitors and catalysis.

3.1 SERS and Sensors

3.1.1 Surface-Enhanced Raman Scattering

SERS is a powerful vibrational spectroscopy technique that can detect low-concentration analytes with high sensitivity by amplifying the electromagnetic fields generated by the excitation of localized surface plasmons [62, 63]. NP Au, Ag and Cu and their composites could be applied for SERS-based sensing to detect amplified Raman signals from active analyte molecules that were adsorbed onto NP metal surfaces due to nanoscale roughness and surface gaps [64–66]. In the study of Chen et al., the effect of pore sizes on the SERS enhancement of NP Au was first investigated by dealloying $Ag_{35}Au_{65}$ using rhodamine 6G (R6G) as the probe [67]. The results demonstrated that smaller pores with a larger surface area could adsorb more probe molecules and produce a stronger SERS enhancement.

Similar results were observed with NP metals prepared by dealloying MGs. In the study of Xue et al., the SERS performance of NP Au was investigated by chemically dealloying Au-based MGs. The Au ligaments can be adjusted to the range of 60–150 nm by tuning the dealloying parameters [35]. As a result, the detection limit could reach 10^{-14} M with the best SERS-active substrate. In addition, various SERS enhancement factors could be achieved by tuning the pore size of NP Au [68–71]. As shown in Fig. 18a, NP Au prepared by electrochemical dealloying of specially designed Ag-based MGs exhibited superior surface-enhanced Raman scattering capacity for R6G molecules [72]. As shown in Fig. 18b, the results of normal Raman experiment suggested that Raman signals of R6G can be detected with a concentration of 10^{-3} mol L^{-1} without any substrate, but its Raman band became invisible when the R6G solution was diluted to 10^{-4} mol L^{-1}. However, the intense characteristic Raman bands of R6G appeared on the surface of the NP Ag substrate at a concentration of 10^{-4} mol L^{-1}.

Wang et al. obtained a low-cost Raman substrate for NP Cu–Ag composites by dealloying Cu–Zr–Al–Ag MGs with different Ag contents [31]. Figure 19 displays the SERS spectra of R6G molecules on the NP Cu and NP Cu–Ag substrates. The SERS intensity increased after the addition of Ag. In particular, NP Cu-Ag prepared by dealloying the $Cu_{50}Zr_{45}Al_5Ag_{10}$ precursor exhibited excellent performance with an EF of 6×10^6 and a sensitive detection property with a detection limit of 10^{-11} mol L^{-1} for R6G. The SERS enhancement of NP Cu–Ag was mainly related to the decrease in the pore size of NP metals due to the addition of Ag, and the stronger SERS effect of silver than copper [25]. However, when the Ag content in the alloy exceeded the composition threshold, an inhomogeneous NP structure was observed, accompanied by obvious cracks and the precipitation of nanoscale particles on the surface of the NP Cu–Ag, leading to a decrease in the number of active sites for stimulating electromagnetic coupling and a reduction of the SERS performance. These results demonstrated that the SERS performance could be efficiently improved by refining pore structure and optimizing the Ag content.

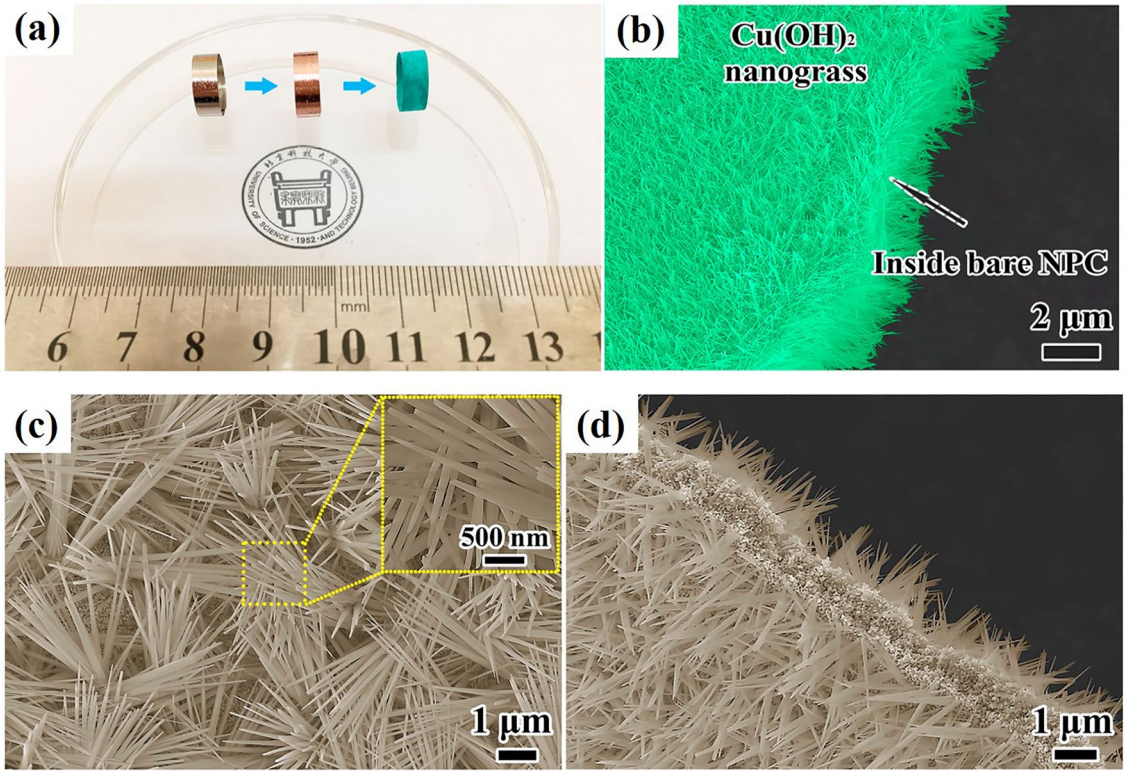

Fig. 14 **a** Digital photograph of a primitive $Cu_{60}Zr_{35}Al_5$ glassy precursor, a dealloyed NP Cu sample and the sample covered with the $Cu(OH)_2$ nanograss structure (left to right). **b** SEM image of an as-prepared free-standing nanohybrid. **c** Surface morphology of the $Cu(OH)_2$ nanograss@NP Cu hybrid. The inset shows an enlarged SEM image of the $Cu(OH)_2$ nanograsses. **d** Cross section of the nanohybrid. Reprinted with permission from [56]

Table 1 lists the sensing performances of the electrochemical sensors based on NP metals for comparison. NP Au, Ag and Cu–Ag all showed excellent SERS performance. Raman hot spots were typically generated at these locations, where local electromagnetic fields were dramatically enhanced due to the resonant excitation of localized surface plasmons. 3D bicontinuous NP metals provided large surface areas for molecule adsorption and hot spots, resulting in the enhancement of the Raman signal. Zhao et al. [73] proposed a novel strategy for the facile preparation of flexible Cu, Cu_3Ag and Cu–Ag NP metals by dealloying Mg–Cu(Ag)–Gd MG ribbons. The Cu and Cu–Ag NP substrates displayed SERS detection limits of 10^{-6} M and 10^{-11} M for R6G, respectively, which are lower than those of most Cu and Cu–Ag substrates prepared by other methods.

3.1.2 Glucose Sensors

Recently, electrochemical sensors have shown great potential as bioprocess monitoring, diabetes management and medical diagnosis. Desirable electrodes of electrochemical glucose sensors should possess high electrical conductivity and high catalytic activity to achieve excellent electrocatalytic performance for glucose detection. NP metals, particularly those consisting of noble metals, are considered as promising candidates. Yang et al. prepared Pd-based NP metals with bicontinuous networks by dealloying metallic Pd–Cu–Ni–P [74]. The NP metals dealloyed from $Pd_{30}Cu_{30}Ni_{20}P_{20}$ with a pore size of 7 nm and a ligament size of 8 nm exhibited the highest oxidation current, demonstrating that the Pd-based NP metals with a smaller pore size displayed a stronger chemical activity toward the direct oxidation reaction of glucose. The Cu_xO or Cu_xO/Ag_2O nanowires were grown on a NP substrate by dealloying Cu-Zr-Ag MGs, followed by anodizing and calcination [61]. The Cu_xO/Ag_2O@NP Cu-Ag electrode exhibited a high sensitivity of 1.31 mA mM^{-1} cm^{-2}, a wide linear range up to 15 mM, outstanding anti-interference ability and stability. The enhanced electrocatalytic performance was mainly ascribed to the synergistic effect of Cu and Ag and their unique structural characteristics. In the study of Li et al., a $Cu(OH)_2$ nanograss array@NP Cu hybrid exhibited a remarkable enhancement in electrocatalytic activity for glucose oxidation [56]. In this case, a cost-effective hierarchical hybrid structure required unique combination of NP Cu with a high conductivity and $Cu(OH)_2$ with a high

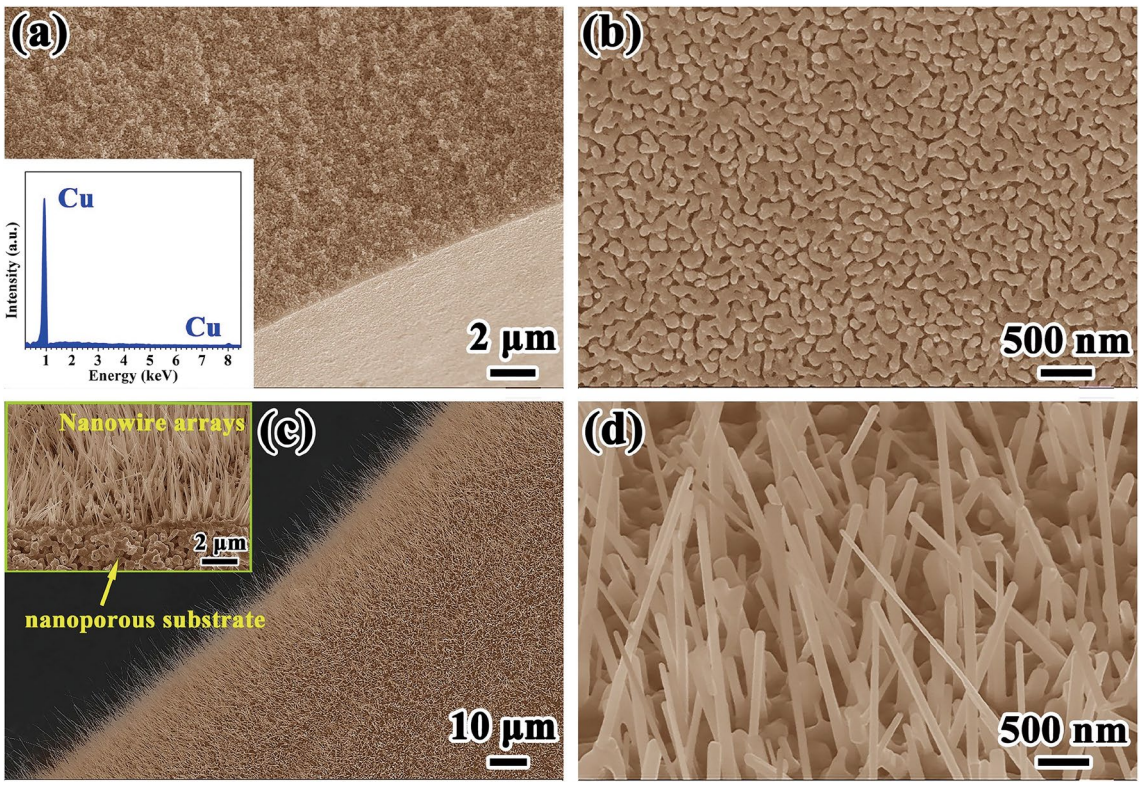

Fig. 15 **a** Cross-sectional morphology and energy-dispersive spectroscopy (EDS) analysis (inset) of the dealloyed NP Cu. **b** Surface morphology of the NP Cu. **c** Overall SEM image of the free-standing CuO nanocomposite. The inset shows the cross-sectional image of the nanocomposite. **d** Surface morphology of the as-prepared CuO nanocomposite. Reprinted with permission from [57]

electrocatalytic activity. As a result, the glucose sensor based on the hybrid nanostructure exhibited extraordinary performance toward glucose oxidation with a high sensitivity of ~ 2.09 mA cm^{-2} mM^{-1}, a wide linear range of 0.2^{-9} mM, a low detection limit of 197 nM, a fast response time below 1 s and excellent selectivity. In addition, a NP Cu thin film was annealed to develop a sandwich-like nanoarchitecture consisting of uniform CuO nanowires array layers grown on a NP Cu_2O film [75]. The glucose sensor based on the CuO/Cu_2O nanocomposite exhibited prominent overall electrocatalytic performance toward glucose oxidation with a wide linear dynamic detection range of 0.1–6 mM, a high sensitivity up to 1.95 mA cm^{-2} mM^{-1}, a short response time below 1.5 s, a low detection limit of 1 mM ($S/N = 3$) and excellent selectivity. The enhanced electrocatalytic properties of the nanocomposite were attributed to the enhanced electrocatalytic activity of the CuO/Cu_2O nanocomposite and its high specific surface area caused by in situ-grown CuO nanowire array structure and synergetic NP Cu_2O framework. The NP NiZrO supported by the $Ni_{64}Zr_{36}$ MG ribbon as a self-supporting electrode can achieve a high sensitivity of 3.19 mA cm^{-2} mM^{-1} in 0.1 M NaOH alkaline solution [76]. Furthermore, the electrochemical results suggested that the electrode exhibited high sensitivity of 4.81 mA cm^{-2} mM^{-1} and high specificity to glucose. The increased sensitivity toward glucose through in situ electrochemical cyclic voltammogram (CV) activation was mainly attributed to the oxidation of the NP NiZrO electrode. These unique properties can be ascribed to the high active surface area and a large number of exposed atoms that promoted the catalytic activity for glucose. To sum up, the above results provide a basis for the future production of enzyme-free glucose sensors related to NP materials and their composites by dealloying MGs.

3.2 Energy Storage

Electrochemical capacitors are urgently needed due to the increasing demand for digital communications, electric vehicles and other devices that require high power in short pulses. High-performance capacitors have widespread uses in the fields of portable electronic devices, hybrid electric vehicles and large industrial equipment [77–79]. Supercapacitors mainly include electric double-layer capacitors and pseudocapacitors. The capacitance of a double-layer capacitor is generated from the charge accumulated at the

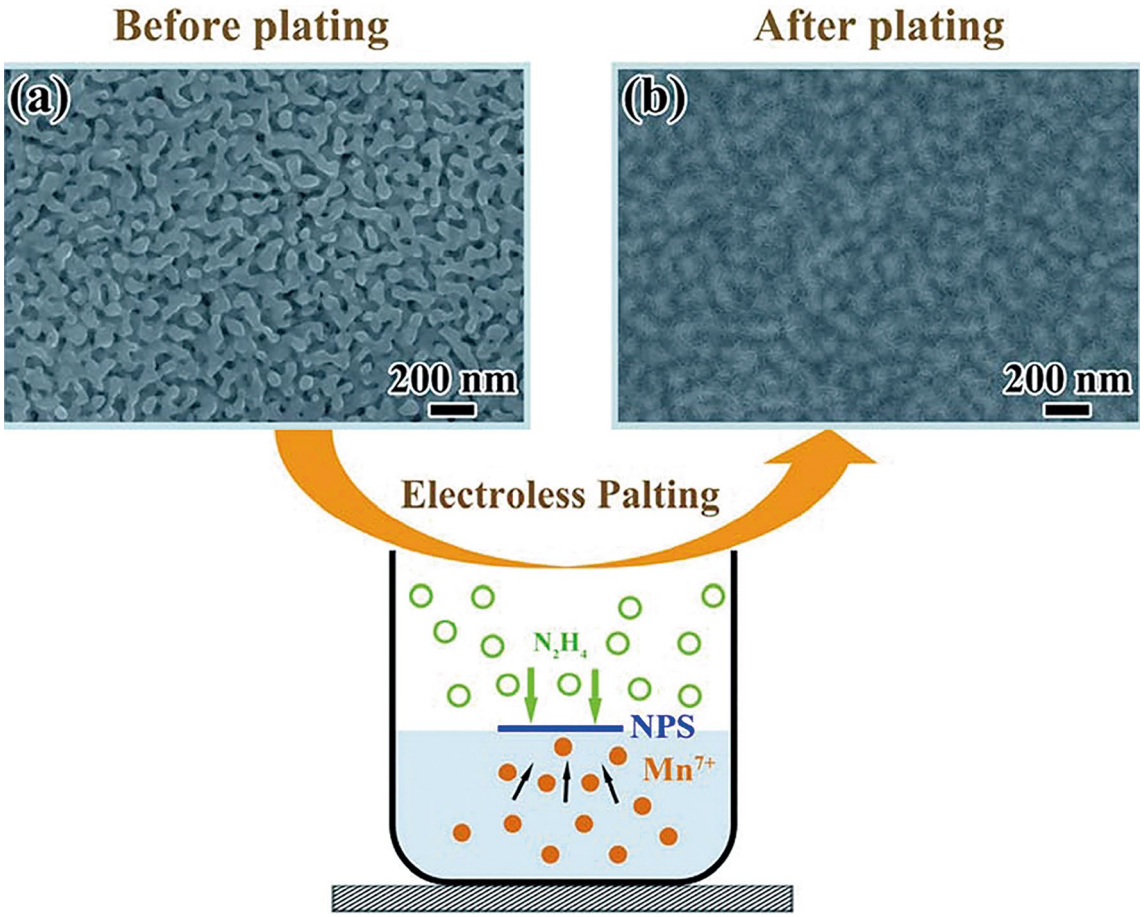

Fig. 16 Schematic of the fabrication process for the NP Ag/MnO_2 composite by electroless plating of MnO_2 into the NP Ag nanopores. **a** Surface SEM image of NP Ag before plating. **b** Surface SEM image of NP Ag after plating. Reprinted with permission from [58]

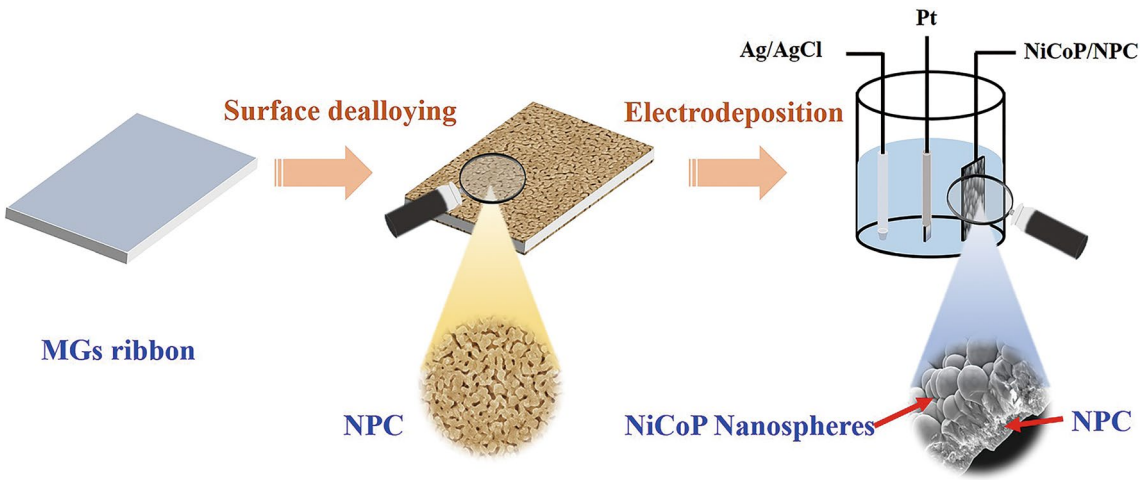

Fig. 17 Schematic illustration of the preparation of the NiCoP/NP Cu nanocomposite. Reprinted with permission from [59]

electrode/electrolyte interface. In contrast, the high energy storage of pseudocapacitors results from charge transfer between electrodes and electrolytes through surface adsorption, reversible faradic redox reactions and ion insertion [80–83]. Transition metal oxides, such as CoO, NiO, RuO_2 and MnO_2, are known as promising supercapacitor

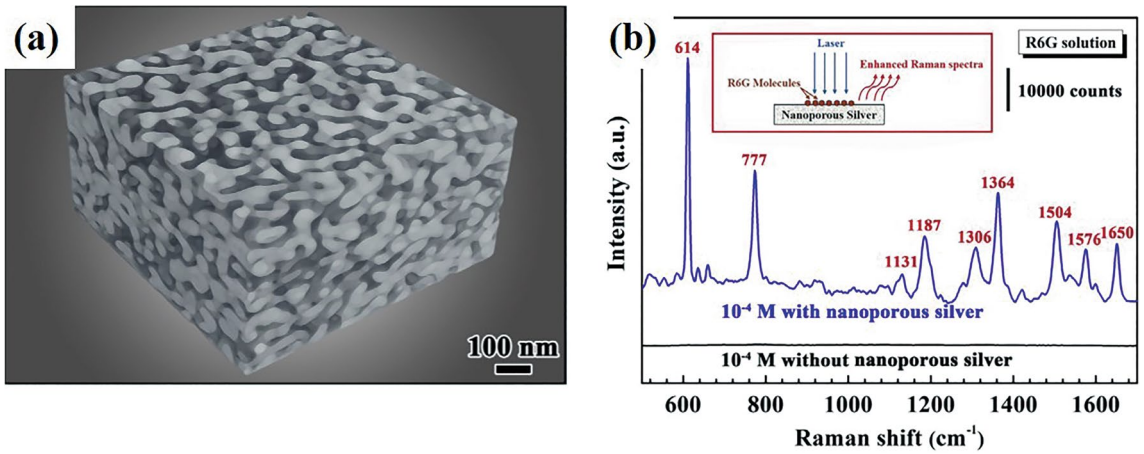

Fig. 18 **a** 3D reconstruction of the cross section of NP Ag by focused ion beam nanotomography. **b** Raman spectra without any substrate and NP silver substrate at 10^{-4} mol L^{-1} R6G. Reprinted with permission from [72]

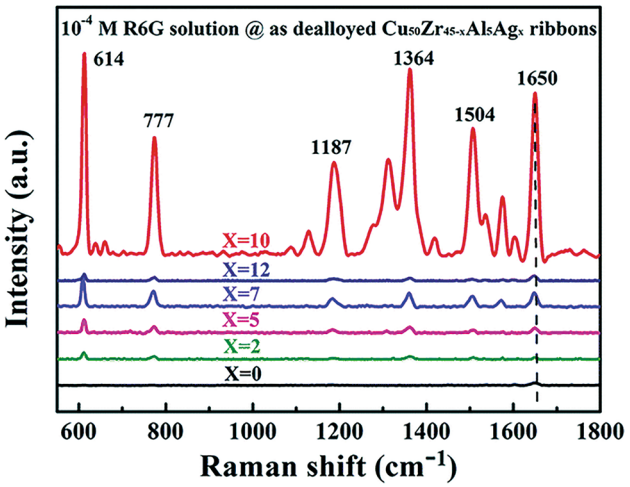

Fig. 19 Raman spectra of the as-dealloyed $Cu_{50}Zr_{45-x}Al_5Ag_x$ ($x=0$, 2, 5, 7, 10 and 12 at.%) ribbons in a 10^{-4} mol L^{-1} R6G solution. Reprinted with permission from [31]

electrode materials. However, the electrical conductivity of catalysts exerts crucial effects on electrode capability. The narrow band gap between the conduction band and valence band of transition metal oxides leads to poor electrical conductivity and low capacitance. In recent years, two strategies have been developed to overcome this deficiency.

External conductive reinforcements by combining with conductive materials, such as carbon [84], conducting polymers [85] and NP metals [86], are capable of enhancing the capacitance. NP metals were employed as supports and collectors for supercapacitor applications due to their open nanopore structure, high surface area and strong interfacial affinity [87, 88]. Li et al. demonstrated that a highly conductive NP Ag network with uniform continuous nanoporosity and high surface area fabricated by dealloying Ag–Mg–Ca MGs can be employed as supports and collectors for MnO_2 capacitors [58]. The SEM image (Fig. 20a) revealed that the NP Ag exhibited a uniform continuous nanoporosity. After the plating process, MnO_2 was uniformly deposited into the nanosized pore structure, resulting in the formation of a porous framework with a rougher surface (Fig. 20b). Figure 19c shows the representative CV curves of the NP Ag bare electrode and NP Ag/MnO_2 composite electrode at a certain scanning rate of 100 mV s^{-1} and different plating time durations (5, 10, 15, 20, 25 and 30 min). The results suggested that the current intensity began to increase with

Table 1 SERS performances of NP metals prepared based on MGs

SERS substrate	Precursor	Probe molecules	Enhancement factor	Detection limit (mol L^{-1})	References
NP Au	$Au_{20}Cu_{48}Ag_7Pd_5Si_{20}$	R6G	–	10^{-7}	[70]
NP Au	$Au_{40}Cu_{28}Ag_7Pd_5Si_{20}$	R6G	–	10^{-8}	[69]
NP Au	$Au_{30}Cu_{38}Ag_7Pd_5Si_{20}$	4,4′-bipyridine	–	10^{-11}	[68]
NP Au	$Au_{20}Cu_{48}Ag_7Pd_5Si_{20}$	4,4′-bipyridine	–	10^{-14}	[67]
NP Ag	$Ag_{45}Mg_{35}Ca_{20}$	R6G	7.59×10^8	10^{-11}	[71]
NP Cu-Ag	$Cu_{50}Zr_{45}Al_5Ag_{10}$	R6G	6×10^6	10^{-11}	[31]

increasing the plating time of MnO_2, but decreased when the plating time exceeded 25 min, which was attributed to the surface morphologies of MnO_2 plating electrodes prepared at different durations. As the plating time increased from 0 to 20 min, the amount of plated MnO_2 increased gradually and the Ag skeletons were uniformly coated by MnO_2 nanocrystals. When the electroplating time was further increased, the excess MnO_2 crystals and clusters blocked the opening channel and hindered the free contact of ions and electrons between MnO_2 and the electrolyte, leading to an obvious decrease in the specific capacitance. Therefore, the NP Ag/MnO_2 composite electrode with the optimized deposition time exhibited fast ion conduction and excellent electron–proton transport performance, resulting in an ultrahigh specific capacitance (~ 1088 F g^{-1}) close to the theoretical limit of active MnO_2 after plating. The unique composite structure endowed the electrode material with excellent cycling ability (Fig. 20d) and high specific capacitance, making the NP Ag/MnO_2 composite a promising electrode material for electrochemical supercapacitors.

In addition, electrical conductivity can be improved by the direct growth of metal oxides on the matrix of NP metals. In the study of Zuo et al., a series of free-standing NP Ni with a novel structure was in situ synthesized by dealloying $Mg_{90-x}Ni_xY_{10}$ ($x = 20$ and 25 at.%) MGs in citric acid solutions [89], and the as-dealloyed samples exhibited a uniform NP structure with a ligament size of about 7 nm. The formed NiO oxidation surface samples were directly applied as binder-free electrodes for the detection of high-performance supercapacitors, and the Ni NPs exhibited excellent reversibility of the redox reaction. When the scanning rate increased to 20 mV s^{-1}, the peak potential difference was only ~ 0.3 V. The specific capacitance was 1.79 F cm^{-2} at a low current density of 1 mA cm^{-2} and remained at 1.58 F cm^{-2} with a high current density of 20 mA cm^{-2}. Meanwhile, charge/discharge cycling at a current density of 20 mA cm^{-2} was conducted to evaluate the cycling stability of the NP Ni. The specific capacitance gradually decreased from 1.58 to 1.1 F cm^{-2} at approximately 1500 cycles and then remained unchanged. The excellent cycling stability was mainly attributed to the direct growth of nanostructured nickel oxide on the conductive metal ligaments.

The NP Ni exhibited a large capacitance due to its high specific surface area. Similarly, Zheng et al. synthesized a sandwich-like NiO/NP Ni/MG composite electrode by dealloying $Ni_{45}Ti_{20}Zr_{25}Al_{10}$ MG ribbons in an O_2-rich HF solution [88]. Unlike conventional free-dealloying, continuous O_2 flow etching in HF allowed in situ growth of NiO microrod arrays on the NP Ni surface. Figure 21a shows the plane-view SEM images of the as-dealloyed $Ni_{45}Ti_{20}Zr_{25}Al_{10}$ MG ribbons after immersion into O_2-rich 0.5 M HF for 60 min at 298 K, and the NiO microrod exhibited a diameter of ~ 500 nm. As shown in Fig. 21b, the CV curves of NiO/NP Ni/MG with different dealloying times at a scan rate of 10 mV s^{-1} indicate that the specific capacitance increased with increasing dealloying time. As shown in Fig. 21c, d, the maximum capacity of the NiO/NP Ni/MG electrode in KOH solution reached 745.3 F cm^{-3} at a current density of 0.5 A cm^{-3}, and exhibited excellent cycling stability under 20 mV s^{-1} with the retention of 92% capacitance after 6000 cycles. In addition, the sandwich structure was designed to provide excellent flexibility for the composite electrode due to the Ni-based MG with high toughness.

Qin et al. reported a novel strategy by one-step dealloying of $Ni_{40}Zr_{20}Ti_{40}$ MG ribbons to synthesize a flexible nickel oxide/hydroxide-coated NP nickel (NP NiO_xH_y@Ni) electrode containing a MG interlayer, denoted as NP NiO_xH_y@Ni/MG/NP NiO_xH_y@Ni sandwich [91]. Due to an integrated sandwich structure and NP NiO_xH_y@Ni shell@core network, the electrode displayed an enhanced capacitance of 778 F cm^{-3} at 1 A cm^{-3} in KOH solutions and achieved 3536 F cm^{-3}. Moreover, the electrode showed a remarkable rate performance of 80.3% retention with a 128-fold increase in the current density, as well as excellent cycle stability of 100% capacitance retention after 8000 cycles. Sun et al. [92] also reported NP Ni@NiO/MG by dealloying $Ni_{40}Zr_{60}$ MG, which exhibited improved flexibility and high electrochemical performance.

CuO has also been widely investigated due to its excellent capacitive performance among transition metal oxides. Li et al. fabricated a flexible three-dimensional NP bimetallic Cu–Ag (NP Cu–Ag) by a simple electrochemical dealloying of $Zr_{45}Cu_{35}Ag_{20}$ glassy ribbon in HF aqueous solution [5]. Moreover, NP CuOAg (NPCuOAg) was prepared by a simple oxidation treatment. As shown in Fig. 22a, NP Cu–Ag exhibited a uniform 3D bicontinuous NP structure, and its surface was uniformly and densely covered with CuO nanosheets after simple oxidation treatment. The CuO nanosheets were perpendicular to the ribbon, indicating that Cu was successfully oxidized to CuO (Fig. 22b). The typical CV curves of the NP CuOAg electrodes showed a rectangular-like shape in the potential range of − 0.3 to 0.4 V (vs. Ag/AgCl) at different scanning rates, as shown in Fig. 22c, indicating that the capacitance of the electrodes resulted from the combination of the double-layer capacitance and faradaic capacity. The nanosheets were grown directly onto the NP Ag skeleton. The nanosheet comprised ultrathin subnanosheets and exhibited rapid electron transfer kinetics and ion diffusion rates at the electrode/electrolyte interface. Therefore, the NP CuOAg electrode exhibited an outstanding capacity of 195.3 mC cm^{-2} at a current density of 1 mA cm^{-2}, as shown in Fig. 22d. It is worth mentioning that the dealloyed ribbon still maintained superior flexibility without any fracture due to the sandwich structure.

In the study of Yang et al., a nonnoble metal (Cu) was introduced into NiCo-based NP metal/metal-oxide

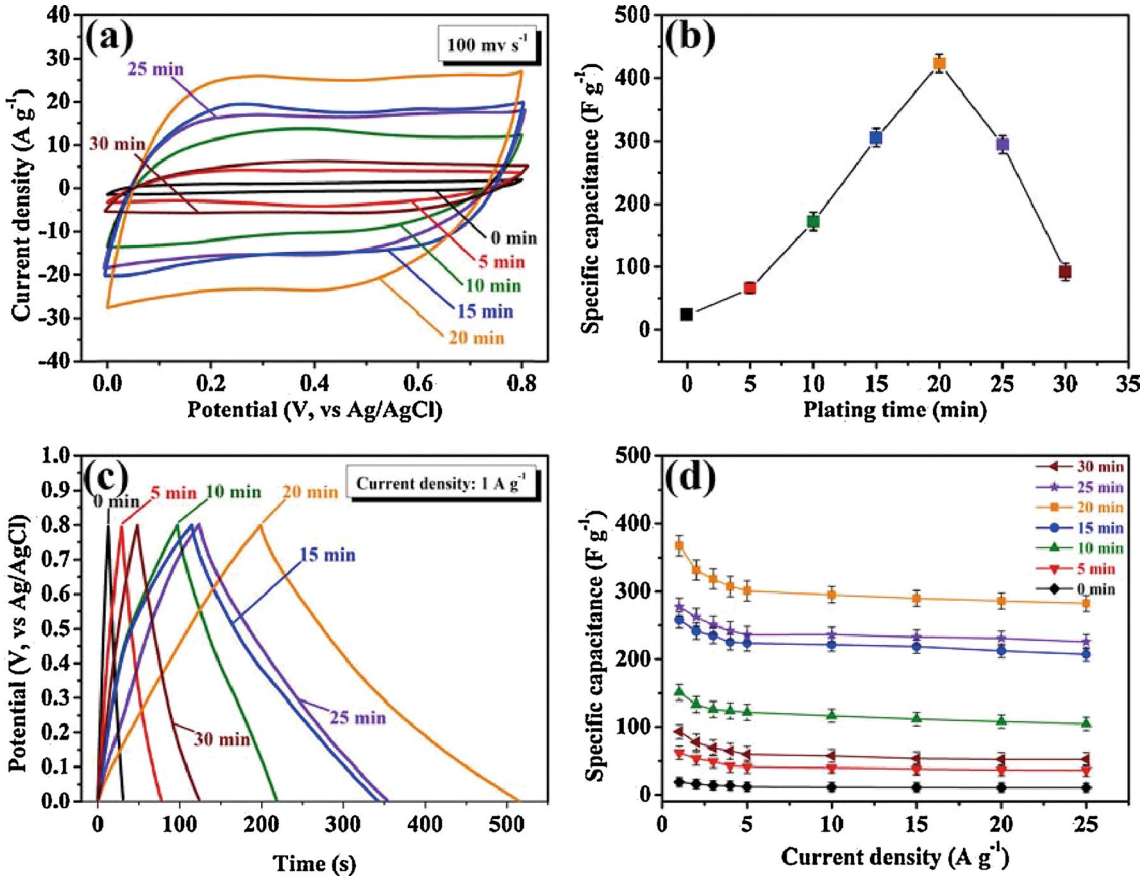

Fig. 20 **a** SEM image of the NP Ag before plating. **b** SEM image of the NP Ag after plating. **c** CV curves for the NP Ag/MnO_2 composite electrodes prepared with different plating times (0–30 min) and a scan rate of 100 mV s^{-1}. **d** The specific capacitance changed as a function of cycle number for the NP Ag/MnO_2 composite electrode plated for 20 min, and the surface morphology of the composite electrode after 1000 cycles (the inset). Reprinted with permission from [58]

composites to decrease their electric resistance and improve their electrochemical capacitance [94]. Yao et al. fabricated NiCo/metal oxide NP composites by one-step dealloying nanocrystallized $Al_{82}Ni_6Co_3Y_6Cu_3$ (at.%) MG ribbons in KOH solution [95]. The capacitance of the dealloyed NP composites reached 3.35 F cm^{-2} (approximately 1522 F cm^{-3}), around 3–10 times that of composites dealloyed from MG and crystalline precursors, which was attributed to the combination of efficient charge transportation rate and high loading of active material. Wang et al. [29] prepared an NPC by dealloying $Cu_{52.5}Hf_{40}Al_{7.5}$ MG with excellent bendability, and the NPC-supported MnO_2 composite electrode displayed significant enhancement in current signal and specific capacitance compared with those of pure MnO_2 powders. NPC substrates with large specific surface areas and excellent electrical conductivity can greatly promote the transformation of MnO_2 from globular particles to nanoflakes with a larger specific surface area and thus improve the utilization of active sites on the MnO_2 surface.

3.3 Electrocatalytic Hydrogen Evolution Reaction (HER)

Sustainable hydrogen production from electrocatalytic water separation has been regarded as one of the most promising methods to obtain renewable and clean energy, owing to its high energy conversion efficiency, simple operation and lack of carbon emissions [96–99]. At present, the noble metal Pt and its composites are considered the most efficient catalysts for the HER, because they can achieve a high current density and almost zero overpotential. However, the high cost and scarcity of Pt limit its widespread use in large-scale hydrogen production [59]. Therefore, it is urgent to develop an earth-abundant, binder-free, efficient catalyst for HER industrial applications [100]. Great efforts have been devoted to developing cost-effective alternatives, particularly for the abundant transition metals (Fe, Co, Ni, Cu, Mn, etc.) and their sulfides, selenides and phosphates [101, 102]. Meanwhile, the HER activity of inexpensive catalysts has been

greatly improved by alloying, nanostructure modification and lattice strain introduction on the surface [103, 104].

Various nanostructured electrocatalysts with high specific surface areas have been developed to show high HER performance. In the study of Zou et al., homogeneous NP Ni particles were developed by ultrasonic-assisted dealloying Mg–Ni–La MG ribbons in a $(NH_4)_2SO_4$ aqueous solution [105]. Particles with different shapes can be fabricated by adjusting the ribbon thickness. Excellent HER activity with a high current density of 100 mA cm^{-2} was achieved by using the particles with a high specific surface area of 53 m^2 g^{-1}, which merely required 46 mV with a small Tafel slope of 21 mV dec^{-1}. However, particle catalysts in practical applications must be attached onto glassy carbons or other types of current collectors through binder additives, which might reduce their activity, stability and conductivity. In this regard, self-supported electrocatalysts are desirable to achieve highly efficient HER.

Free-standing 3D NP materials have then drawn much attention due to their outstanding performance in catalysis [106–109]. The uniform and bicontinuous nanoporosity prepared by dealloying can offer NP materials satisfactory electrocatalytic activities, high-efficiency electron transportation and improved selectivity for various redox reactions. Numerous NP materials, especially NP transition metals and their oxides, have been reported as efficient catalysts for the HER/oxygen evolution reaction (OER) in electrolytes. Wang et al. altered the shape of MG precursors to achieve hierarchically porous structures by introducing residual stresses on the surface [40]. The NP Ni/MG wire with a hierarchically porous structure was prepared by one-step surface dealloying of the designed Ni-based MG wires. The porous composite was composed of micron gaps and nanopores interleaving, which increased the effective surface area of the catalytic reaction and facilitated the hydrogen release. As a result, the NP Ni/MG hybrid electrode exhibited prominent HER performance with a low overpotential of 78 mV at 10 mA cm^{-2} and a Tafel slope of 42.4 mV dec^{-1} (Fig. 23a and b), as well as outstanding stability in alkaline solutions.

Alloying is another important approach to improving catalytic activities and introducing new functions of heterogeneous catalysts, which have been extensively employed in

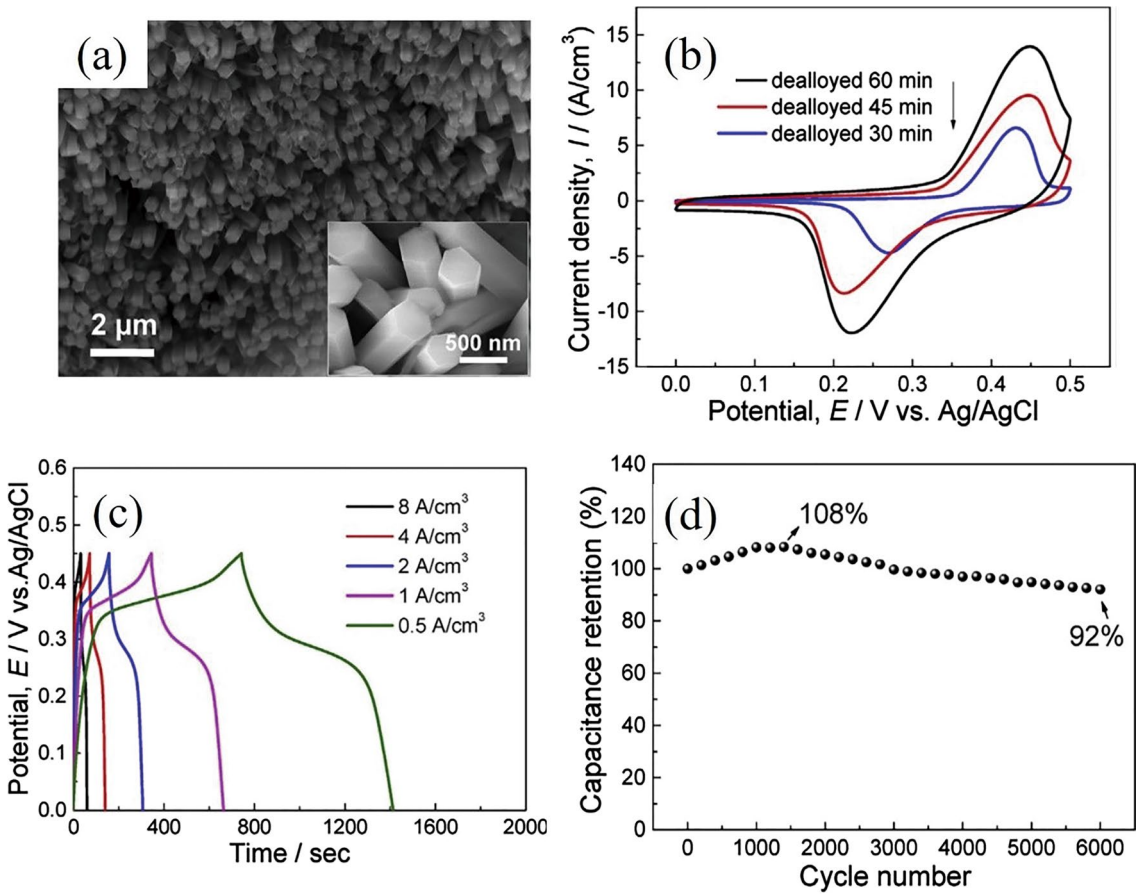

Fig. 21 **a** SEM image of NiO/NP Ni/MG. **b** CV curves of the samples dealloyed for 30, 45 and 60 min measured at a scan rate of 10 mV s^{-1}. **c** Charge/discharge curves of the sample immersed in 0.5 mol L^{-1} HF solution for 60 min at 298 K. **d** Volume capacitance as a function of cycle number at a sweep rate of 20 mV s^{-1} in 1 mol L^{-1} KOH solution. Reprinted with permission from [90]

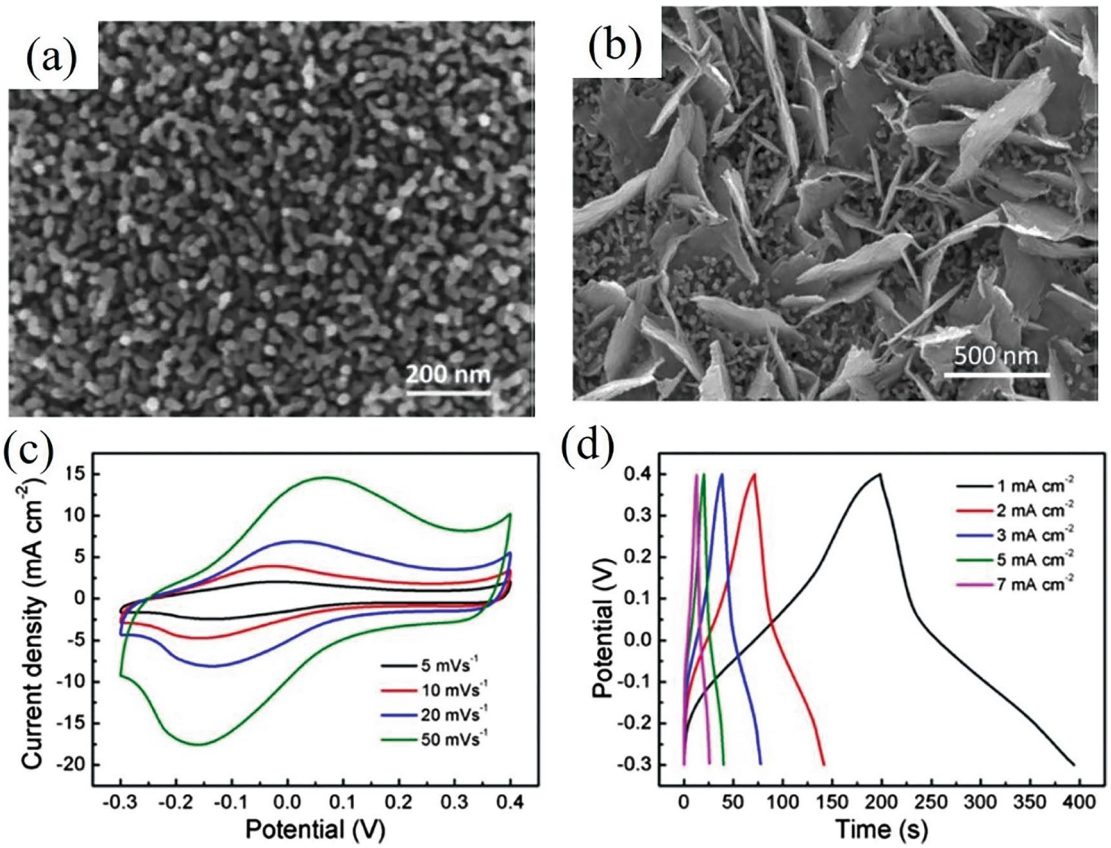

Fig. 22 **a** SEM image of NP CuOAg. **b** High-magnitude SEM image. **c** CV figures of the NP CuOAg electrode at different scan rates. **d** Galvanostatic charge/discharge curves of the NP CuOAg electrode at different current densities. Reprinted with permission from [93]

the fabrication of bimetallic catalysts. Li et al. fabricated a honeycombed NP Pt(Ni)/glassy sandwich structure by dealloying Ni-based MG, as shown in Fig. 13a [55]. A honeycombed $Pt_{75}Ni_{25}$ solid solution NP structure was formed on the dealloyed MG surface by adding only 3 at.% Pt into the MG precursor, showing increased effective active sites and a large area for HER contact to achieve cost reduction. As shown in Fig. 13b, $Ni_{40}Zr_{40}Ti_{20}$ MG ribbon with bi-continuous pores and ligaments was obtained through etching in 0.025 mol L^{-1} HF for 30 min at room temperature. In addition, a honeycombed structure was created on the surface of $Ni_{40}Zr_{40}Ti_{17}Pt_3$ MG under the same etching conditions (Fig. 13b).

In addition, the compressive lattice-strain effect was also introduced on the catalyst surface to reduce the hydrogen adsorption energy due to the replacement of Pt lattice sites with smaller Ni atoms, which could be clarified by density functional theory (DFT) calculations. As shown in Fig. 24, the Pt (top) site on the $Pt_{75}Ni_{25}$ (111) surface exhibited the smallest $|\Delta GH^*|$ value of 0.127 eV among the modeled $Pt_{75}Ni_{25}$ (111) surfaces, much lower than that of the optimal Ni (111) hcp site (0.223 eV) and Pt (111) top site (0.185 eV). Therefore, the $Pt_{75}Ni_{25}$ surface possesses much higher HER activity than Ni or Pt. The synergistic effects of the nanostructure surface and the substitutional solution endowed the hybrid electrocatalyst with a quite small overpotential of 37 mV at 10 mA cm^{-2} and a low Tafel slope of 30 mV dec^{-1} in alkaline media, which was superior to the commercial Pt/C catalyst. This work not only offers a reliable strategy to develop cost-effective and flexible multicomponent catalysts with low Pt usage for efficient HER, but also sheds light on understanding the alloying effects of the catalytic process.

Moreover, Li et al. [110] reported a physical-metallurgy-based structural design strategy to develop a self-supporting unique NP structure with core–shell-like ligaments. Specifically, alloy metals with constituent elements having positive mixing enthalpy were introduced to the precursors, and the core–shell structure was created by phase separation during the chemical dealloying process. A NP Cu core surrounded by a NiO shell was formed on the MG substrate by alloying Cu into the Ni–Zr–Ti MG precursor, as shown in Fig. 25. The unique core–shell-structured catalyst exhibited excellent HER activity due to the integration of the high conductivity of Cu core and the large catalytic activity of Ni/NiO shell. The overpotential reached 67 mV at a current density of 10 mA cm^{-2}, accompanied by a low Tafel

slope of 40 mV dec^{-1} and outstanding durability. This work highlights the structural design strategy via phase separation to synthesize core–shell nanocatalysts with desirable electrocatalytic performance. Zhu et al. [111] reported a facile dealloying method based on MG ($Ni_{61}Zr_{36}Mo_3$) to introduce abundant oxygen vacancies for the electrocatalytic HER. The corroded ribbons consisted of a sandwich-like structure with a Ni–Mo–O NP layer outside and raw MG inside, which exhibited a low overpotential of 71 ± 2.6 mV at -20 mA cm^{-2} geo in 1 mol L^{-1} KOH solution, a Tafel slope of 57 ± 3 mV dec^{-1} and 100 h long-term stability for the HER, outperforming those of the crystallized counterpart, NP Ni and the commercial benchmark 20% Pt/C electrocatalyst Jiang et al. [112] likewise pointed out the importance of alloying effects in improving the performance of electrocatalysts. The results indicated that NP Ni–Co-P exhibited outstanding electrocatalytic performance for the HER with a low overpotential of 114 mV at a current density of 10 mA cm^{-2}, a small Tafel slope (57.3 mV dec^{-1}) and extraordinary long-term durability in 1 mol L^{-1} KOH, which was attributed to the NP structure, disordered atomic arrangement and alloying effects. The synergetic effect of Ni and Co improved the intrinsic activity of the active sites, and the introduced transition metallic element Fe and nonmetallic elements P and C were conducive to preparing NP amorphous PdFePC with outstanding HER catalytic activity and long-term stability.

Electrodes consisting of multiple elements have attracted wide interest since the synergistic effect between different elements may endow superior catalytic activity [113]. The study of Ju et al. first reported the fabrication of a NiCoMnYAu multicomponent NP catalyst with excellent catalytic activity in acidic solutions [114]. The regional EDS images (Fig. 26a, b) confirmed that the nanoligaments consisting of Au, Ni, Co, Mn and Y alloys were uniformly dispersed in Au. The thin AuNiCo-rich layer at the interface between the MG and NP layer was attributed to the enhancement of the corrosion resistance in acidic electrolytes and high stability. Thus, the existence of various elements probably gave rise to a synergistic effect during the catalytic reaction, and enhanced the HER activity with 70 mV at 10 mA cm^{-2} and a Tafel slope of approximately 39 mV dec^{-1} (Fig. 25c, d). The catalyst performance continuously improved over time because Al elements in the amorphous matrix were dissolved into the solution during the constant current process, resulting in the exposure of active sites to improve catalytic activity. The study of Jia et al. indicates that the lattice distortion, chemical complexity and synergism of high-entropy alloys (HEAs) accelerated the adsorption/desorption of H^+ [115]. Therefore, nanosponge-like PdPtCuNiP high-entropy MG with ample active sites was achieved by surface dealloying and exhibited a greater HER activity with η10 (32 mV) than most currently available catalysts in KOH (Fig. 27a–e).

Interestingly, high-activity catalysts can be composited with conductive materials. In the study of Li et al., NiCoP with a high activity and NP Cu with a high conductivity were combined to fabricate a self-supporting NiCoP/NP Cu composite by electrochemical deposition of NiCoP microspheres on NP Cu [59]. The substrate endowed desirable conductivity and provided a highly even structure, which promoted the uniform nucleation of NiCoP and prevented the aggregation of deposited NiCoP. Moreover, the self-supported structural design of NiCoP/NP Cu eliminated the additional electrical resistance of binders, enabling a better electrical connection and electron transport. As a result, the NiCoP/NP Cu-35 catalyst exhibited superior HER activity with a low overpotential of 80 mV at 10 mA cm^{-2} and a Tafel slope of 48.9 mV dec^{-1}, along with superior stability

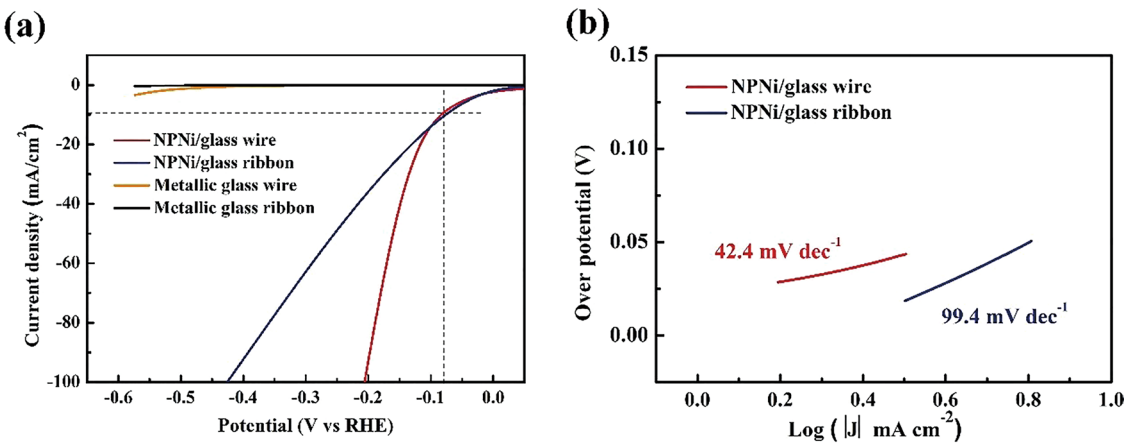

Fig. 23 **a** Polarization curves and **b** Tafel plots of NP Ni/MG wire and NP Ni/MG ribbon for HER with iR compensation in 1 mol L^{-1} KOH. Reprinted with permission from [40]

in alkaline solutions. In terms of application, the facile method for creating transition metal phosphides supported by NP Cu has the potential to be extended in other areas as well.

3.4 Electrocatalytic OER

The electrocatalytic OER is an important half reaction for electrochemical energy conversion, including water splitting, CO_2 reduction and N_2 reduction. However, active electrocatalysts are required to overcome the reaction energy barrier to accelerate the dynamics. Recently, MGs and their composites have been proven to be highly efficient electrocatalysts toward the OER under both acidic and alkaline conditions.

Qian et al. [116] reported a NP NiFeMoP by dealloying $Ni_{45}Fe_{40}Mo_{10}P_5$ precursor ribbons in the 1 M HNO_3, which showed good catalytic activity with a low overpotential of 197 mV at 20 mA cm^{-2} for the OER in the 1 mol L^{-1} KOH. The enhanced catalytic activities were originated from the continuous NP structure that increases the specific surface area and promotes electron transfer, as well as the addition of metal phosphide and $Ni_xFe_{1-x}OOH$ that enhances the ribbon strength and offers prominent electrochemical stability. In addition, amorphous/nanocrystal composites were also used as precursors to fabricate NP metals during the dealloying process. In the study of Chen et al. [117], NP Fe was easily fabricated using Fe-based MG ribbons to prepare Fe-based nanocrystalline alloys as precursors after chemical dealloying in HCl solution, showing prominent OER performance with an overpotential of 230 mV at a current density of 10 mA cm^{-2}. Similarly, amorphous/nanocrystal ribbons were employed as precursors for dealloying to obtain NP metals with improved catalytic activity [118, 119]. As a result, not only amorphous but also amorphous/nanocrystalline composites can be used as precursors for the preparation of porous metals, which provides additional pathways for the design of high-performance porous metals for a wide range of applications.

Another strategy for enhancing the catalyst performance is to obtain copious high-energy atomic steps at the interface by controlling the solidification behavior of glass-forming metallic liquids to improve the OER performance. This approach not only greatly improved the catalyst activity but also eliminated the dealloying step to simplify the process. Li et al. [120] pointed out that highly faceted $FeNi_3$ nanocrystals could be in situ synthesized in Fe–Ni–B MG matrix by regulating the chemical composition and cooling rate, resulting in the generation of ordered/disordered interfaces, as shown in Fig. 28a–c. Owing to the catalytic activity and stable atomic step at the jagged interfaces, the resultant free-standing $FeNi_3$ nanocrystal/MG composite exhibited a low oxygen-evolving overpotential of 214 mV at 10 mA cm^{-2}, a small Tafel slope of 32.4 mV dec^{-1}, and excellent stability in alkaline media, which was superior to most state-of-the-art catalysts (Fig. 28e–h). Amorphous/nanocrystalline composites prepared by physical metallurgy can be used directly as electrodes, and the process

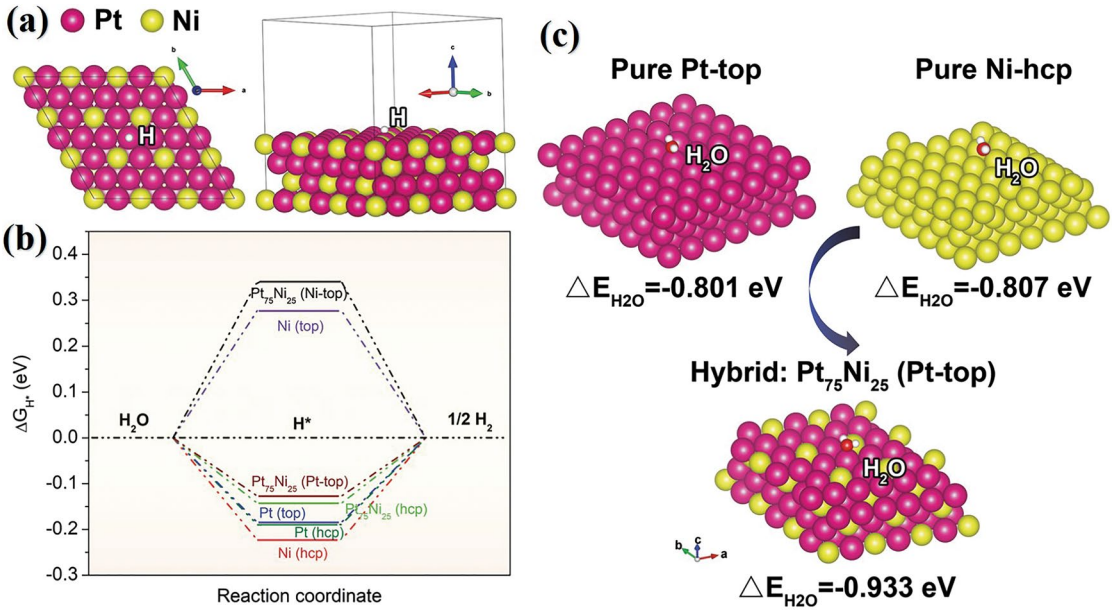

Fig. 24 Theoretical calculations. **a** Atomic configuration of the $Pt_{75}Ni_{25}$ (Pt-top) model and the adsorption site of H*. **b** Calculated free-energy changes in different models. **c** Water adsorption energies for the Ni hcp, Pt top and $Pt_{75}Ni_{25}$ (Pt-top) models. Reprinted with permission from [55]

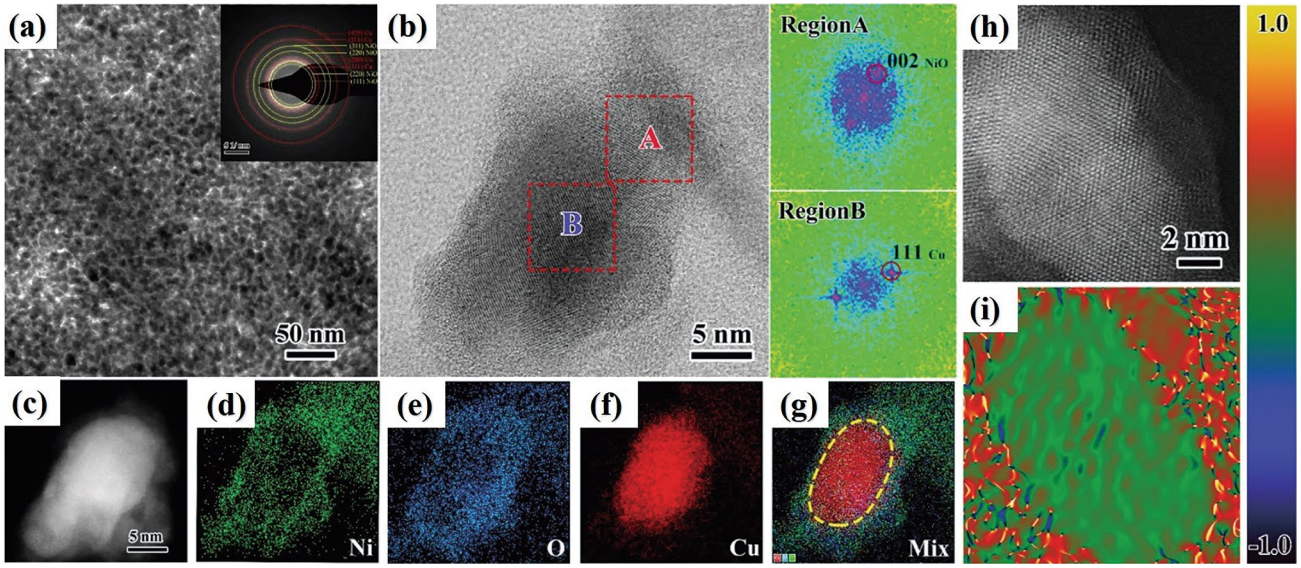

Fig. 25 Structural characterization of the core–shell-structured NP Cu@(Ni/NiO)/MGs. **a** Bright-field TEM image of NP $Cu_{25}Ni_{25}$. The inset shows the SAED pattern. **b** HRTEM images of NP $Cu_{25}Ni_{25}$. **c–g** High-angle annular dark field-STEM images of NP $Cu_{25}Ni_{25}$ and the corresponding EDS elemental maps. **h**, **i** HRTEM image of NP $Cu_{25}Ni_{25}$ and strain distribution of *exx*. (The compressive strain is represented by the color from green to dark blue, while the tensile strain is represented by the color from red to bright yellow.) [110]

of preparing electrodes is made simpler by removing the de-alloying step.

In addition, NP metals prepared by dealloying MG precursors have great application prospects in other fields, such as mechanical properties [121], sono-Fenton-like catalytic performance [29], oxidation of formic acid [49, 122, 123], oxidation of HCHO [124], ethanol oxidation [125] and wastewater treatment [117].

4 Concluding Remarks and Perspectives

4.1 Scientific Issues

From the above literature review, we can see that various high-performance NP metals can be designed using MGs as precursors, and the chemical composition, pore and electronic structures of NP metals can be tuned through the control of MG design and dealloying conditions. However, there is a lack of an in-depth understanding of the relationship between MG precursors and the resultant porous structures. Moreover, the chemical composition-porous structure–property relationship is also unclear. In order to reveal the formation mechanism of NP metals and the synergistic coupling effect of porous structure and chemical composition, to achieve the precise regulation of porous structure and to establish a design guideline for high-performance NP metals, the following key scientific issues still need to be addressed.

4.1.1 Formation Mechanisms of NP metals

The precise modulation of pore and electronic structures of NP metals is indispensable to achieve desirable properties. Therefore, it is necessary to understand nanoporosity formation mechanisms. In principle, the development of porous structures is mainly affected by the chemical composition of MG precursors and the dealloying condition. However, MG precursors are often comprised of multiple constituent elements, and thus, the complex chemical interaction between the constituent elements makes the dealloying process complicated and challenging. Concurrently, dealloying parameters such as the dealloying solution, temperature and time play a crucial role in the formation of porous structures and ligament size. Obviously, the complexity of MG precursors and the diversity of dealloying conditions make the design of precursor alloys and the regulation of porous structures more difficult. To reveal the formation mechanism of NP metals, we need to systematically investigate the effects of MG composition and dealloying conditions on the porous structure.

4.1.2 Design and Regulation of NP Alloys with Hierarchical Pore Structures

The strong alloying effect in multicomponent NP alloys has a significant impact on their electronic structures and renders them prominent functional properties. In addition, the hierarchical pore structure possesses some unique properties, e.g., it could be a possible solution to overcome the activity-stability trade-off of electrocatalysts, such as a

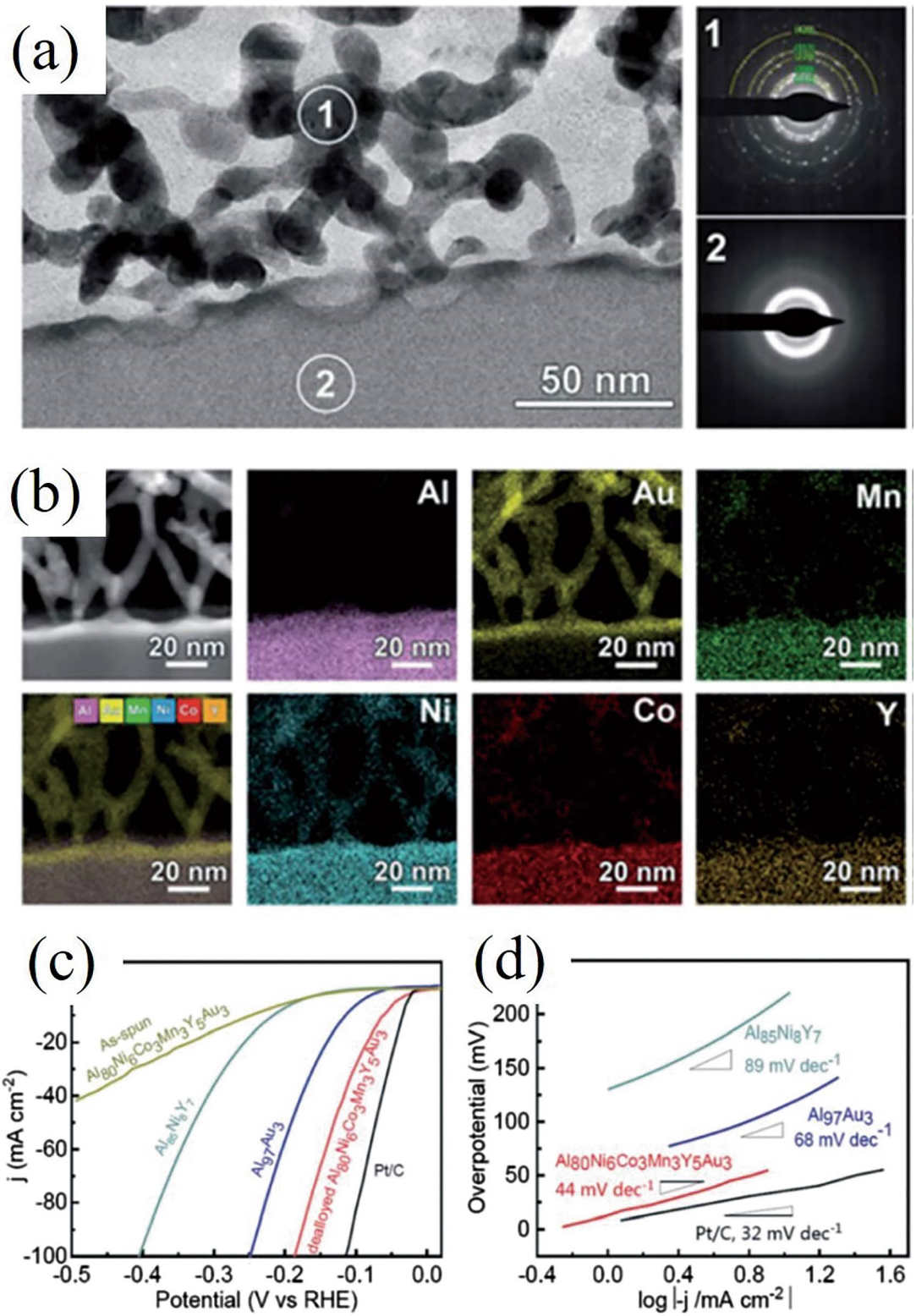

Fig. 26 **a** TEM image of the amorphous matrix and the porous surface layer with the diameter of the nanoligaments and nanopores of approximately 10 nm. The SAED diffraction rings of the porous layer confirm the nanocrystalline structure, and the SAED pattern of the matrix shows a typical characteristic of amorphous phases with a diffraction halo. **b** High-angle annular dark field (HAADF) image and EDS map confirming the dissolution of Al during the reaction and the formation of Au ligaments with uniformly distributed Co, Ni, Mn and Y. **c** Polarization curves measured at a scan rate of 5 mV s^{-1}. **d** Tafel plots for the $Al_{85}Ni_7Y_8$, $Al_{97}Au_3$, $Al_{80}Ni_6Co_3Mn_3Y_5Au_3$ and Pt/C electrodes derived from the HER polarization curves. Reprinted with permission from [114]

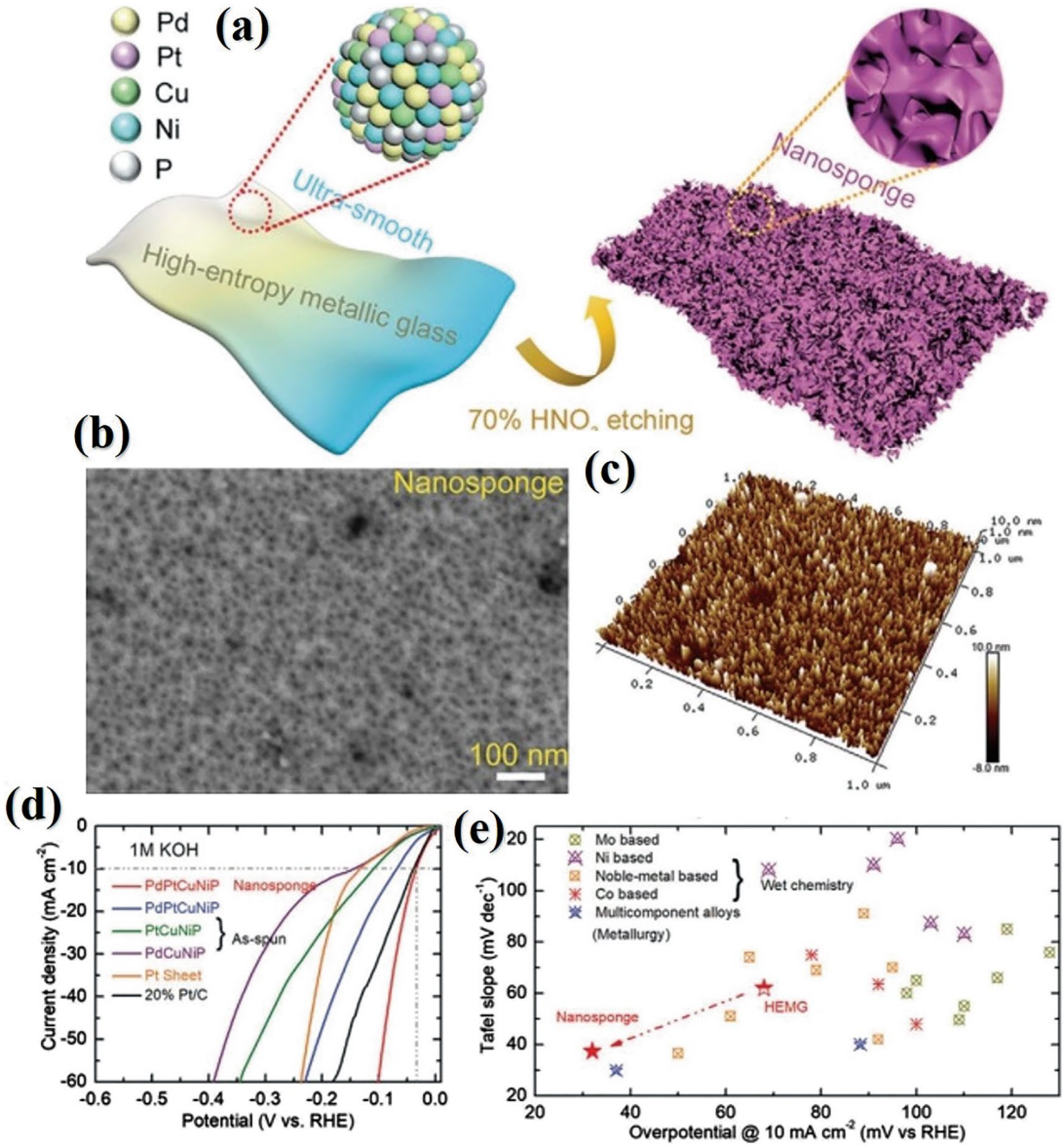

Fig. 27 **a** Schematic illustration of the preparation process of the nanosponge-like high-entropy metallic glasses (HEMGs). **b** SEM and **c** 3D AFM images of the dealloyed HEMG ribbon surface. **d** Polarization curves of the as-spun and dealloyed HEMGs in 1 mol L^{-1} KOH solution. **e** Comparison of HER activities with recently reported electrocatalysts in 1 mol L^{-1} KOH solution [115]

hierarchical porous structure by Li et al. [126] developed via dealloying HEA, which was used as the high-efficiency water splitting electrocatalyst. Therefore, how to design multicomponent NP alloys with hierarchical structures is particularly important to develop new porous materials with superior performance. However, the porous structure and chemical composition of multicomponent NP alloys are difficult to precisely modulate through dealloying treatments due to their chemical complexity. In particular, the design of hierarchical structures is more challenging than conventional NP structures, because it requires consideration of both the microstructure of precursor alloys and its evolution during the dealloying process. Therefore, the intrinsic correlation between MG precursors and NP alloys with hierarchical structures needs to be further investigated. This will reveal the formation mechanism and establish guidelines for the design of hierarchically structured NP alloys with superior performance.

4.1.3 Composition-Porous Structure–Property Relationship

The relationship between chemical composition, porosity and functional properties is fundamental in designing novel porous metals or alloys with desirable attributes. The

appropriate combination of constituent elements in MG precursors directly influences the formation and stability of these porous structures. Understanding the intricate relationship between composition, the resulting porous structure and the material's properties allows researchers to optimize and customize nanoporous metals for a variety of applications, such as in energy storage, electrochemical devices and catalysis. In particular, a systematic study of the intrinsic correlation between alloying, hierarchical porous structures and properties (e.g., electrocatalytic performance) is needed to clarify the synergistic coupling effect of alloying and hierarchical porous structures and the underlying physical mechanisms. Despite significant progress, several challenges remain in understanding and optimizing the composition-porous structure–property relationships in these advanced materials. One critical obstacle is controlling the morphology and homogeneity of the porous structure during dealloying processes, which can profoundly influence the material's functional properties. Moreover, the development of robust and consistent synthesis methods for tailoring a wide array of metal compositions is still elusive, limiting the exploration of new material systems for specific applications.

4.2 Perspectives

In order to gain a comprehensive understanding of the three key scientific questions mentioned above and promote the development and practical applications of porous metals, we propose that future research should focus on the following three primary aspects:

4.2.1 Advanced Characterization Techniques and Computer Simulations

Understanding the formation mechanisms of NP metals remains a significant challenge. To address this issue, advanced characterization techniques must be developed to determine the influence of alloying and dealloying conditions on the porous and electronic structures. Hence, it is crucial to integrate cutting-edge in situ characterization techniques (such as in situ X-ray absorption spectroscopy, differential electrochemical mass spectrometry and transmission electron microscopy (TEM)) and computer simulations (such as first-principles calculation and molecular dynamics) to systematically investigate the effects of alloying and dealloying conditions on porous structure formation and its mechanisms.

Future research should concentrate on multicomponent porous materials with hierarchical structures due to their synergistic effects on improving overall performance. To fundamentally comprehend the coupled synergistic impacts of alloying and hierarchical structures, accurate and simple theoretical models for computation are required. These calculations can be employed as an aid to verify active catalytic sites, electronic structures and strain effects for the synthesis of high-performance porous metals. Furthermore, advanced in-situ characterization techniques should be refined to unravel the detailed structure–component–activity relationship that accounts for the intriguing catalytic mechanisms of multicomponent porous materials with hierarchical structures, as well as to study the catalytic mechanisms and deactivation evolution processes of NP materials.

4.2.2 Machine Learning and High-Throughput Techniques

A number of alloy components are available for choosing from as a result of the multicomponent composition of porous materials. Utilizing traditional trial-and-error methods for alloy design will result in substantial workloads. Therefore, it is beneficial to implement machine learning-based theoretical predictions for alloy component design together with high-throughput experimental techniques to facilitate efficient and rapid screening of alloy component designs. In this regard, future research should focus on developing data-driven machine learning approaches to reveal the intricate composition-porous structure–property relationship.

4.2.3 Devise Application-Driven Studies

Developing new preparation methods is essential to produce cost-effective and highly active NP catalysts on a large scale, conforming to industrial standards and regulations. Additionally, considering the recyclability and service life of these catalysts is crucial. Exploring highly active NP catalysts for various significant catalytic reactions, such as nitrogen reduction for fertilizer production and carbon hydrogenation for fuel production, is imperative. The application of NP catalysts in energy storage and conversion devices, including but not limited to, water splitting, fuel cells, carbon dioxide reduction (CO_2RR) for fuel productions, rechargeable hydrogen gas batteries and metal-air batteries should be further advanced to emphasize the importance of NP materials in catalysis. In development of innovative fabrication methods to produce NP metals and alloys, scalability and reproducibility should also be considered.

By focusing on these key aspects, future research will undoubtedly pave the way for a new era of NP metal science and technology, potentially leading to groundbreaking innovations in various industry sectors.

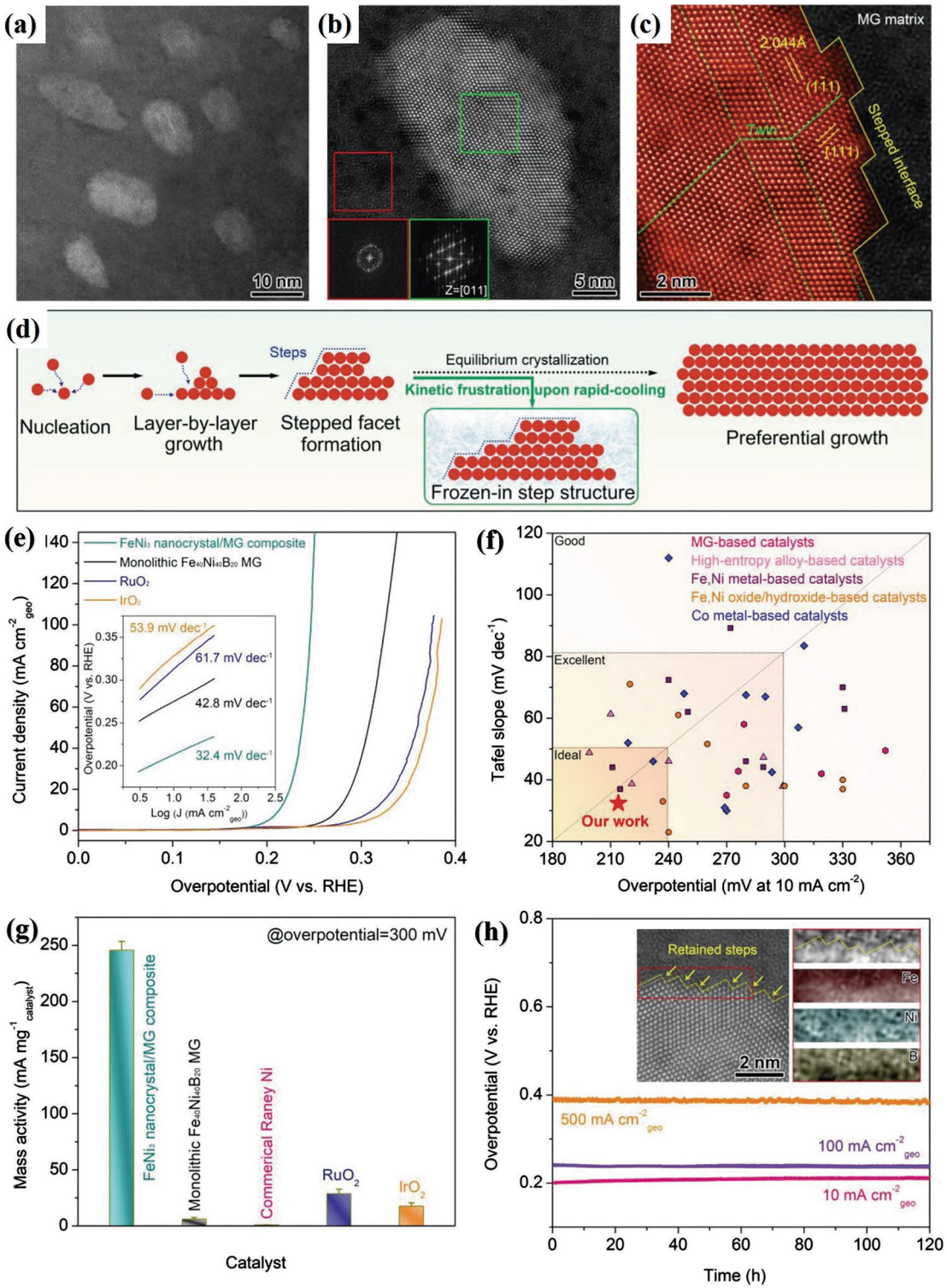

Fig. 28 Structure and formation mechanism of the atom-stepped interfaces. **a** HR-TEM image of the as-spun $Fe_{40}Ni_{40}B_{20}$ MG composite with in situ-precipitated $FeNi_3$ nanocrystals. **b** HAADF-STEM image and the fast Fourier transformation patterns of the selected areas (the insets) of the $FeNi_3$ nanocrystal. **c** Atomic structure of the stepped interface between the twinned $FeNi_3$ nanocrystal and MG matrix. **d** Schematic illustration of the formation process of the stepped interface architecture during the rapid solidification. **e** OER polarization curves of the as-spun monolithic $Fe_{40}Ni_{40}B_{20}$ MG, $FeNi_3$ nanocrystal/MG composite, and commercial IrO_2 and RuO_2 catalysts in 1 mol L^{-1} KOH electrolyte. The inset shows the corresponding Tafel plots of these catalysts. **f** Comparison of the OER activity of the as-spun $FeNi_3$ nanocrystal/MG composite with various recently reported state-of-the-art transition metal-based electrocatalysts in alkaline. **g** Mass activities of the catalysts at an overpotential of 300 mV. Error bars represent the standard deviation from five independent measurements. **h** Chrono-potentiometric curves were recorded at 10, 100 and 500 mA cm^{-2} for the composite catalyst. The inset shows the atomic structure of the stepped interface after 120 h at the high current density of 500 mA cm^{-2} and the electron energy loss spectroscopy elemental mapping of the selected area. [120]

Acknowledgements This research was supported by the National Natural Science Foundation of China (Nos. 52071024, 52271003, 52101188), the Funds for Creative Research Groups of NSFC (51921001), the Projects of International Cooperation and Exchanges of NSFC (51961160729, 52061135207), the 111 Project (BP0719004), the Program for Changjiang Scholars and Innovative Research Team in University of China (IRT_14R05), and the Fundamental Research Fund for the Central Universities of China (FRF-TP-22-005C2).

Declarations

Conflict of interest The authors state that there are no conflicts of interest to disclose.

References

[1] Y. Ding, M.W. Chen, MRS Bull. **34**, 569 (2009)
[2] J.S. Yu, Y. Ding, C.X. Xu, A. Inoue, T. Sakurai, M.W. Chen, Chem. Mater. **20**, 4548 (2008)
[3] J.R. Hayes, A.M. Hodge, J. Biener, A.V. Hamza, K. Sieradzki, J. Mater. Res. **21**, 2611 (2006)
[4] M. Hakamada, M. Mabuchi, J. Alloy. Compd. **479**, 326 (2009)
[5] J. Weissmüller, K. Sieradzki, MRS Bull. **43**, 14 (2018)
[6] Z. Qi, C.C. Zhao, X.G. Wang, J.K. Lin, W. Shao, Z.H. Zhang, X.F. Bian, J. Phys. Chem. C **113**, 6694 (2009)
[7] X.G. Wang, Z. Qi, C.C. Zhao, W.M. Wang, Z.H. Zhang, J. Phys. Chem. C **113**, 13139 (2009)
[8] H. Lechtman, Sci. Am. **250**, 56 (1984)
[9] R. Murray, U. S. Patent. **1628**, 190 (1927)
[10] H. Pickering, P. Swann, Corrosion **19**, 373t (1963)
[11] I.C. Oppenheim, D.J. Trevor, C.E. Chidsey, P.L. Trevor, K. Sieradzki, Science **254**, 687 (1991)
[12] R.C. Newman, K. Sieradzki, Science **263**, 1708 (1994)
[13] K. Sieradzki, R.C. Newman, U. S. Patent **4**, 977 (1990)
[14] L.Y. Chen, J.L. Kang, Y. Hou, P. Liu, T. Fujita, A. Hirataa, M.W. Chen, J. Mater. Chem. A **1**(32), 9202 (2013)
[15] F. Kertis, J. Snyder, L. Govada, S. Khurshid, N. Chayen, J. Erlebacher, JOM **62**, 50–56 (2010)
[16] Q. Chen, Y. Ding, M.W. Chen, MRS Bull. **43**, 43 (2018)
[17] Y. Hou, L.Y. Chen, L. Zhang, J.L. Kang, T. Fujita, J.H. Jiang, T.S. Fujita, J.H. Jiang, M.W. Chen, J. Power Sources **225**, 304 (2013)
[18] R.Q. Yao, X.Y. Lang, Q. Jiang, J. Iron Steel Res. Int. **119**, 1 (2019)
[19] H.J. Qiu, L. Peng, X. Li, H.T. Xu, Y. Wang, Corros. Sci. **92**, 16 (2015)
[20] G.J. Li, X.P. Song, Z.B. Sun, S.C. Yang, B.J. Ding, S. Yang, Solid State Sci. **13**, 1379 (2011)
[21] D.M. Artymowicz, J. Erlebacher, R.C. Newman, Philos. Mag. **89**, 1663 (2009)
[22] Y. Ding, Y.J. Kim, J. Erlebacher, Adv. Mater. **16**, 1897 (2004)
[23] J.R. Hayes, A.M. Hodge, J. Biener, A.V. Hamza, K. Sieradzki, J. Mater. Res. **21**, 2611 (2011)
[24] C.C. Zhao, Z. Qi, X.G. Wang, Z.H. Zhang, Corros. Sci. **51**, 2120 (2009)
[25] J. Erlebacher, M.J. Aziz, A. Karma, N. Dimitrov, K. Sieradzki, Nature **410**, 450 (2001)
[26] Z.H. Dan, F.X. Qin, Y. Sugawara, I. Muto, N. Hara, J. Alloy Compd. **557**, 166 (2013)
[27] Z.H. Zhang, Y. Wang, Z. Qi, W.H. Zhang, J.Y. Qin, J. Frenzel, J. Phys. Chem. C **113**, 12629 (2009)
[28] E. Paschalidou, F. Celegato, F. Scaglione, P. Rizzi, L. Battezzati, A. Gebert, S. Oswald, U. Wolff, L. Mihaylov, T. Spassov, Acta Mater. **119**, 177 (2016)
[29] N. Wang, Y. Pan, S.K. Wu, E.M. Zhang, W.J. Dai, RSC Adv. **7**, 43255 (2017)
[30] Z. Deng, C. Zhang, L. Liu, Intermetallics **52**, 9 (2014)
[31] J. Wang, X.J. Liu, R. Li, Z.B. Li, X.Z. Wang, H. Wang, Y. Wu, Z.P. Lu, Inorg. Chem. Front. **7**, 1127 (2020)
[32] R. Li, N. Wu, J.J. Liu, Y. Jin, X.B. Chen, T. Zhang, Corros. Sci. **119**, 23 (2017)
[33] H. Xu, T. Zhang, Corros. Sci. **153**, 1 (2019)
[34] S.S. Wang, C. Zhang, H. Li, L. Liu, Intermetallics **87**, 6 (2017)
[35] Y.P. Xue, F. Scaglione, P. Rizzi, L. Battezzati, Appl. Surf. Sci. **426**, 1113 (2017)
[36] Y. Xue, F. Scaglione, P. Rizzi, L. Battezzati, Corros. Sci. **127**, 141 (2017)
[37] T. Aburada, J.M. Fitz-Gerald, J.R. Scully, Corros. Sci. **53**, 1627 (2011)
[38] R. Li, X. Liu, H. Wang, Y. Wu, Z.P. Lu, Corros. Sci. **104**, 227 (2016)
[39] R. Li, X.J. Liu, H. Wang, D.Q. Zhou, Y. Wu, Z.P. Lu, Acta Mater. **105**, 367 (2016)
[40] J. Wang, L. You, Z. Li, X.J. Liu, R. Li, Q. Du, Mater. Sci. Technol. **73**, 145 (2021)
[41] M. Zhang, M.P. Li, T. Yin, T. Zhang, Mater. Lett. **162**, 273 (2016)
[42] X. Wang, R. Li, Z. Li, R.J. Xiao, X.B. Chen, T. Zhang, J. Mater. Chem. B **7**, 4169 (2019)
[43] Y.W. Tan, H. Wang, P. Liu, Y.H. Shen, C. Cheng, A. Hirata, F. Takeshi, Z. Tang, M.W. Chen, Energy Environ. Sci. **9**, 2257 (2016)
[44] W. Jiao, P. Liu, H. Lin, W. Zhou, Z. Wang, T. Fujita, A. Hirata, H.W. Li, M.W. Chen, Chem. Mater. **29**, 4478 (2017)
[45] J.C. Thorp, K. Sieradzki, L. Tang, P.A. Crozier, A. Misra, M. Nastasi, Appl. Phy. Lett. **88**, 033110 (2006)
[46] L. Sun, C.L. Chien, P.C. Searson, Chem. Mater. **16**, 3125 (2004)
[47] A. Kloke, F. von Stetten, R. Zengerle, S. Kerzenmacher, Adv. Mater. **23**, 4976 (2011)
[48] S.L. Ou, D.G. Ma, Y.H. Li, K. Yubuta, Z.Q. Tan, Y.M. Wang, W. Zhang, J. Alloy. Compd. **706**, 215 (2017)
[49] Y.Q. Zeng, S.C. Yang, H. Xiang, X. Dong, L. Chen, M. Chen, Intermetallics **61**, 66 (2015)
[50] S. Tanaka, T. Kaneko, N. Asao, Y. Yamamoto, M.W. Chen, W. Zhang, Chem. Commun. **47**, 5985 (2011)
[51] X.Y. Lang, H. Guo, L.Y. Chen, A. Kudo, J.S. Yu, W. Zhang, J. Phys. Chem. C **114**, 2600 (2010)
[52] L.H. Qian, M.W. Chen, Appl. Phy. Lett. **91**, 083105 (2007)
[53] G. Andreasen, M. Nazzarro, J. Ramirez, R.C. Salvarezza, A.J. Arvia, J. Electrochem. Soc. **143**, 466 (1996)
[54] Z.H. Dan, F.X. Qin, Y. Sugawara, I. Muto, A. Makino, N. Hara, Mater. Lett. **94**, 128 (2013)
[55] R. Li, X.J. Liu, R.Y. Wu, J. Wang, Z.B. Li, K.C. Chan, Adv. Mater. **31**, e1904989 (2019)
[56] R. Li, X. Liu, H. Wang, Y. Wu, Z. Lu, Biosens. Bioelectron. **102**, 288 (2018)
[57] R. Li, K.C. Chan, X.J. Liu, X.H. Zhang, L. Liu, T. Li, Corros. Sci. **126**, 37 (2017)
[58] R. Li, X. Liu, H. Wang, Y. Wu, Z.P. Lu, Electrochi. Acta **182**, 224 (2015)
[59] Z.B. Li, J. Wang, X.J. Liu, R. Li, H. Wang, Y. Wu, Scr. Mater. **173**, 51 (2019)
[60] Y. Li, C. Ji, Y.C. Chi, Z.H. Dan, H.F. Zhang, F.X. Qin, Acta Metall. Sin. Engl. Lett. **32**, 63 (2018)
[61] Q. Zhang, M. Li, Z.F. Wang, C.L. Qin, M.M. Zhang, Y.Y. Li, Appl. Surf. Sci. **515**, 15 (2020)
[62] B. Sharma, R.R. Frontiera, A.I. Henry, E. Ringe, R.P. Van Duyne, Mater. Today **15**, 16 (2012)

[63] F. Feng, G. Zhi, H.S. Jia, L. Cheng, Y.T. Tian, X.J. Li, Nanotechnology **20**, 295501 (2009)
[64] L.Y. Chen, J.S. Yu, T. Fujita, M.W. Chen, Adv. Funct. Mater. **19**, 1221 (2009)
[65] K. Liu, Y.C. Bai, L. Zhang, Z.B. Yang, Q. Fan, H.Q. Zheng, Nano Lett. **16**, 3675 (2016)
[66] Y. Jiao, J.D. Ryckman, P.N. Ciesielski, C.A. Escobar, G.K. Jennings, S.M. Weiss, Nanotechnology **22**, 295302 (2011)
[67] L.H. Qian, X.Q. Yan, T. Fujita, A. Inoue, M.W. Chen, Appl. Phys. Lett. **90**, 153120 (2007)
[68] Y.P. Xue, F. Scaglione, E.M. Paschalidou, P. Rizzi, L. Battezzati, Chem. Phys. Lett. **665**, 6 (2016)
[69] F. Scaglione, E.M. Paschalidou, P. Rizzi, S. Bordiga, L. Battezzati, Phil. Mag. Lett. **95**, 474 (2015)
[70] Y.P. Xue, E.M. Paschalidou, P. Rizzi, L. Battezzati, P. Denis, H.J. Fecht, Phil. Mag. **98**, 2769 (2018)
[71] Y.P. Xue, F. Scaglione, F. Celegato, P. Denis, H.J. Fecht, P. Rizzi, Chem. Phys. Lett. **709**, 46 (2018)
[72] R. Li, X.J. Liu, H. Wang, Y. Wu, X.M. Chu, P.Z. Lu, Corros. Sci. **84**, 159 (2014)
[73] Y. Zhao, F. Qian, C. Zhao, C. Xie, J. Wang, C. Chang, Y. Li, L. Zhang, J. Mater. Sci. Technol. **70**, 205 (2021)
[74] C.L. Yang, X.H. Zhang, G. Lan, L.Y. Chen, M.W. Chen, Y.Q. Zeng, Chinese Chem. Lett. **25**, 496 (2014)
[75] R. Li, X.J. Liu, H. Wang, Y. Wu, K.C. Chan, Z.P. Lu, Electrochi. Acta **299**, 470 (2019)
[76] X. Di, Y. Pan, W.J. Dai, Y.A. Zhu, T. Lu, Mater. Lett. **271**, 127694 (2020)
[77] J.R. Miller, P. Simon, Science **321**, 651 (2008)
[78] C.G. Liu, Z.N. Yu, D. Neff, A. Zhamu, B.Z. Jang, Nano Lett. **10**, 4863 (2010)
[79] R. Kötz, M. Carlen, Electrochi. Acta **45**, 2483 (2000)
[80] M. Winter, R.J. Brodd, Chem. Rev. **10**, 104 (2004)
[81] A.G. Pandolfo, A.F. Hollenkamp, J. Power Sources **157**, 11 (2006)
[82] L.B. Hu, J.W. Choi, Y. Yang, S. Jeong, F. La Mantia, L.F. Cui, P. Natl, Acad. Sci. USA **106**, 21490 (2009)
[83] Y. Wang, Z.Q. Shi, Y. Huang, Y.F. Ma, C.Y. Wang, M.M. Chen, J. Phys. Chem. C **113**, 13103 (2009)
[84] F. Cai, Y.R. Kang, H.Y. Chen, M.H. Chen, Q.W. Li, J. Mater. Chem. A **2**, 11509 (2014)
[85] D.S. Patil, J.S. Shaikh, S.A. Pawar, R.S. Devan, Y.R. Ma, A.V. Moholkar, Phys. Chem. Chem. Phys. **14**, 11886 (2012)
[86] G.Q. Zhang, H.B. Wu, H.E. Hoster, M.B. Chan-Park, X.W.D. Lou, Energ. Environ. Sci. **5**, 9453 (2012)
[87] L.Y. Chen, J.L. Kang, Y. Hou, P. Liu, T. Fujita, A. Hirata, J. Mater. Chem. A **1**, 9202 (2013)
[88] X.Y. Lang, H.T. Yuan, Y. Iwasa, M.W. Chen, Scr. Mater. **64**, 923 (2011)
[89] L. Zuo, R. Li, Y. Jin, H.J. Xu, T. Zhang, J. Electrochem. Soc. **164**, A348 (2017)
[90] D.H. Zheng, F. Zhao, Y.Y. Li, C.L. Qin, J.S. Zhu, Q.F. Hu, Electrochim. Acta **297**, 767 (2019)
[91] C.L. Qin, D.H. Zheng, Q.F. Hu, X.M. Zhang, Z.F. Wang, Y.Y. Li, Appl. Mater. Today **19**, 100539 (2020)
[92] X. Sun, D. Zheng, F. Pan, C. Qin, Y. Li, Z. Wang, Y. Liu, Appl. Surf. Sci. **545**, 149043 (2021)
[93] H.Y. Li, S.S. Wang, L. Liu, Z.W. Zhang, Y. Yu, L. Liu, J. Electrochem. Soc. **165**, A947 (2018)
[94] H. Yang, H.J. Qiu, J.Q. Wang, J.T. Huo, X.M. Wang, R.W. Li, J. Alloy. Compd. **703**, 461 (2017)
[95] A. Yao, H. Yang, J.Q. Wang, W. Xu, J.T. Huo, R.W. Li, J. Alloy. Compd. **772**, 164 (2019)
[96] S. Chu, A. Majumdar, Nature **488**, 294 (2012)
[97] T.Y. Wang, H. Xie, M.J. Chen, A. D'Aloia, J. Cho, G. Wu, Nano Energy **42**, 69 (2017)
[98] A. Eftekhari, Int. J. Hydrogen Energ. **42**, 11053 (2017)
[99] F. Yu, H.Q. Zhou, Z. Zhu, J.Y. Sun, R. He, J.M. Bao, S. Chen, Z.F. Ren, ACS Catal. **7**, 2052 (2017)
[100] J.R. McKone, S.C. Marinescu, B.S. Brunschwig, J.R. Winkler, H.B. Gray, Chem. Sci. **5**, 865 (2014)
[101] Y. Jiao, Y. Zheng, M. Jaroniec, S.Z. Qiao, Chem. Soc. Rev. **44**, 2060 (2015)
[102] Q.Q. Zhou, T.T. Li, J.Y. Wang, F.Y. Guo, Y.Q. Zheng, Electrochim. Acta **296**, 1035 (2019)
[103] S.Y. Tee, K.Y. Win, W.S. Teo, L.D. Koh, S. Liu, C.P. Teng, Adv. Sci. **4**, 1600337 (2017)
[104] M.H. Shao, J.H. Odell, A. Peles, D. Su, Chem. Commun. **50**, 2173 (2014)
[105] L. Zuo, R. Li, Y. Jin, T. Zhang, J. Electrochem. Soc. **165**, F207 (2018)
[106] A.J. Welch, J.S. DuChene, G. Tagliabue, A. Davoyan, W.H. Cheng, H.A. Atwater, A.C.S. Appl, Energy Mater. **2**, 164 (2018)
[107] Z.Y. Tu, M.J. Zachman, S. Choudhury, S.Y. Wei, L. Ma, Y. Yang, Adv. Energy Mater. **7**, 1602367 (2017)
[108] Y. Ito, W. Cong, T. Fujita, Z. Tang, M.W. Chen, Angew. Chem. Int. Edit. **127**, 2159 (2015)
[109] R.Q. Yao, Y.T. Zhou, H. Shi, Q.H. Zhang, L. Gu, Z. Wen, ACS Energy Lett. **4**, 1379 (2019)
[110] Z.B. Li, R.Y. Wu, Y.R. Wu, F.K. Chiang, X.J. Liu, J. Wang, R. Li, H. Wang, Y. Wu, S.H. Jiang, X.Z. Wang, Z.P. Lu, Nanoscale **14**, 325 (2022)
[111] Y.A. Zhu, Y. Pan, W. Dai, T. Lu, A.C.S. Appl, Energy Mater. **3**, 1319 (2020)
[112] R. Jiang, Z. Cui, W. Xu, S. Zhu, Y. Liang, Z. Li, S. Wu, C. Chang, A. Inoue, Electrochim. Acta **328**, 135082 (2019)
[113] Y.G. Yao, Z.N. Huang, P.F. Xie, S.D. Lacey, R.J. Jacob, H. Xie, F.J. Chen, A. Nie, T.C. Pu, M. Rehwoldt, D.W. Yu, M.R. Zachariah, C. Wang, R. Shahbazian-Yassar, J. Li, L.B. Hu, Science **359**, 1489 (2018)
[114] S. Ju, J.Q. Feng, P. Zou, W. Xu, S.J. Wang, W.B. Gao, H.J. Qiu, J.T. Huo, J.Q. Wang, J. Mater. Chem. A **8**, 3246 (2020)
[115] Z. Jia, K. Nomoto, Q. Wang, C. Kong, L. Sun, L.C. Zhang, S.X. Liang, J. Lu, J.J. Kruzic, Adv. Funct. Mater. **31**, 2101586 (2021)
[116] H. Qian, K. Li, X. Mu, J. Zou, S. Xie, X. Xiong, X. Zeng, Int. J. Hydrogen Energ. **45**, 16447 (2020)
[117] S. Chen, M. Li, Q. Ji, X. Chen, S. Lan, T. Feng, K. Yao, J. Non-Cryst, Solids. **571**, 121070 (2021)
[118] S. Jiang, L. Zhu, Z. Yang, Y. Wang, Int. J. Hydrogen Energ. **46**, 36731 (2021)
[119] Y. Jin, G. Xi, R. Li, Z. Li, X. Chen, T. Zhang, J. Alloy. Compd. **852**, 156876 (2021)
[120] R. Li, R. Wu, Z. Li, J. Wang, X. Liu, Y. Wen, F.K. Chiang, S.W. Chen, K.C. Chan, Z. Lu, Adv. Mater. (2022). https://doi.org/10.1002/adma.202206890
[121] C. Wang, S. Zhu, Y. Liang, Z. Cui, S. Wu, C. Qin, S. Luo, A. Inoue, J. Mater. Sci. Technol. **53**, 91 (2020)
[122] Y. Zeng, S. Yang, H. Xiang, X. Dong, L. Chen, M. Chen, A. Inoue, X. Zhang, J. Jiang, Intermetallics **61**, 66 (2015)
[123] Y. Zeng, J. Zhang, X. Dong, X. Zhang, J. Jiang, Mater. Res. Innov. **20**, 7333 (2017)
[124] Y. Jin, R. Li, L. Zuo, T. Zhang, J. Alloy. Compd. **695**, 1600 (2017)
[125] Z. Dan, F. Qin, T. Wada, S. Yamaura, G. Xie, Y. Sugawara, I. Muto, A. Makino, N. Hara, Electrochim. Acta **108**, 512 (2013)
[126] R. Li, X.J. Liu, W.H. Liu, Z.B. Li, K.C. Chan, Z.P. Lu, Adv. Mater. **9**, 2105808 (2022)